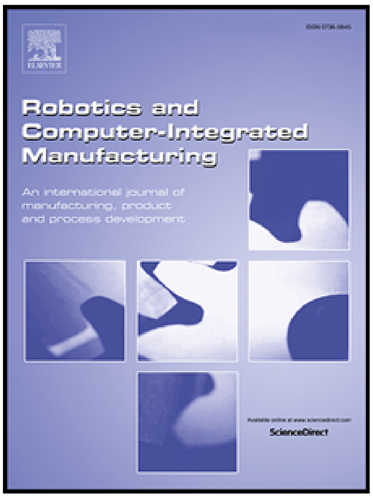

Kinematical and dynamical modelling of a multipurpose upper limbs rehabilitation robot

Aitziber Mancisidor, Asier Zubizarreta, Itziar Cabanes,
Pablo Bengoa, Je Hyung Jung

PII: S0736-5845(16)30209-5
DOI: 10.1016/j.rcim.2017.08.013
Reference: RCM 1569

To appear in: *Robotics and Computer–Integrated Manufacturing*

Received date: 16 June 2016
Revised date: 13 August 2017
Accepted date: 14 August 2017

Please cite this article as: Aitziber Mancisidor, Asier Zubizarreta, Itziar Cabanes, Pablo Bengoa, Je Hyung Jung, Kinematical and dynamical modelling of a multipurpose upper limbs rehabilitation robot, *Robotics and Computer–Integrated Manufacturing* (2017), doi: 10.1016/j.rcim.2017.08.013

Highlights

- A model of the robot is essential to design proper and safe controllers.
- The kinematical and dynamical models of the UHP robot have been identified.
- The UHP is an innovative multipurpose rehabilitation robot for upper limbs.
- Several experimental test have been carried out to validate the identified models.
- Results show that the models can be used for force and motion estimation.

Kinematical and dynamical modelling of a multipurpose upper limbs rehabilitation robot

Aitziber Mancisidor[a], Asier Zubizarreta[a], Itziar Cabanes[a,*], Pablo Bengoa[a], Je Hyung Jung[b]

[a]Department of Automatic Control and Systems Engineering, University of the Basque Country (UPV/EHU), Plaza Ing. Torres Quevedo, Bilbao 48013, Spain
[b]Neurorehabilitation Area, Health Division, TECNALIA Research and Innovation, Mikeletegi Pasealekua 1-3, Donostia-San Sebastian 20009, Spain

Abstract

Knowing accurate model of a system is always beneficial to design a robust and safe control while allowing reduction of sensors-related cost as the system outputs are predictable using the model. In this context, this paper addresses the kinematical and dynamical model identification of the multipurpose rehabilitation robot, Universal Haptic Pantograph (UHP), and present experimental validations of the identified models. The UHP is a pantograph based innovative robot actuated by two SEAs (Series Elastic Actuator), aiming at training impaired upper limbs after a stroke. This novel robot, thanks to its lockable/unlockable joints, can change its mechanical structure so that it enables stroke patient to perform different training exercises of the shoulder, elbow and wrist. This work focuses on the ARM mode, which is a training mode used to rehabilitate elbow and shoulder. The kinematical model of UHP is identified based on the loop vector equations, while the dynamical model is derived based on the Lagrangian formulation. To demonstrate the accuracy of the models, several experimental tests were performed. The results reveal that the mean position error between estimated values with the model and actual measured values stays in 3 mm (less than 2% of the maximum motion range). Moreover,

---

*Corresponding author
Email addresses: `itziar.cabanes@ehu.eus` (Itziar Cabanes), `jehyung.jung@tecnalia.com` (Je Hyung Jung)

the error between estimated and measured interaction force is smaller than 10% of maximum force range. So, the developed models can be adopted to estimate motion and force of UHP as well as control it without the need of additional sensors such as a force sensor, resulting in the reduction of total robot cost.

Keywords: Upper limb rehabilitation, Rehabilitation robots, Kinematical modelling, Dynamical modelling, Force estimation, Experimental validation.

1. Introduction

According to the World Health Organization (WHO), every year, more than 15 million strokes or cerebrovascular accidents are diagnosed and two thirds among them survive but have to live with the sequels of stroke. Nowadays, more than 33 million people in the world are affected by stroke sequels [1, 2]. Up to date, various research results on stroke have demonstrated that, thanks to brain plasticity, stroke patients may recover most of their skills executing adequate rehabilitation exercises [3]. However, in classical rehabilitation programs, stroke patients require constant supervision by the therapist, which increases the economic cost of the therapy, and leads to the reduction of rehabilitation times, impeding continuous and long-term rehabilitation interventions [4].

Hence, over the last couple of decades, several rehabilitation robotic devices for stroke patients, particularly for upper limbs rehabilitation, have been developed [5, 6] and demonstrated at both academical and clinical settings. The robots are believed to be a good alternative to traditional rehabilitation therapies due to several advantages of the robot-mediated therapy [7]: 1) robots emulate and replicate the movements produced by a physiotherapist, executing longer duration, higher frequency and better accuracy treatments; 2) with the objective of evaluating the progress of the patient as well as adapting the exercises to their needs, the device can act as a measurement tool that quantifies forces and/or movements; 3) using a graphical interface, a virtual reality environment can be built, facilitating patient involvement in the rehabilitation process.

The rehabilitation robotic devices can be classified into two groups: end-effector type and wearable type (exoskeleton). The MIT-Manus [8], MIME [9], GENTLE/s [10], REHAROB [11] belong to the end-effector type while Armin [12], L-Exos [13], RUPERT [14] or Limpact [15] fall into the wearable type. Differently from other robotics areas where the usual position control strategies are used with great success, rehabilitation robots should take into account the interaction between the patient and the robot, and use it so as to safely apply assistive force to the patient during trainings. This indicates that it is necessary to implement advanced control algorithms that combine motion and force measurements [16]. In the literature, several approaches such as force control [17], computed torque control [18], algorithms using EMG signals [19] or neuro-fuzzy control [20] have been proposed to control the patient-robot interaction. Among the proposed approaches, impedance control introduced by Hogan in 1984 [21], and its complimentary method, admittance control, have been the most common [22, 23].

In order to implement these advanced controllers, an appropriate kinematical and dynamical model of the robot is required. This model determines the human-robot interaction forces and its motion, and force transmission between the actuators and the interaction point [24, 25]. Moreover, in order to implement the control law, the actual position and force exerted to the patient need to be not only motorized but also sensorised continuously. However, direct force measurement requires force sensors that add mechanical and electrical complexity to the mechanical structure. In addition, these sensors are normally very expensive compared to other components such as motor [26], resulting in unaffordable price of robots. Such unaffordability is one of main barriers that impede wide use of the rehabilitation robots.

Accurate models of the robot can be used to implement estimators of both position and force as an alternative of direct measurement using the sensors in order to reduce the cost of the robot. Normally, these estimators use the easily measurable variables and elements information provided by manufactures (e.g. actuator specifications) to estimate the motion and forces of the robots [27, 28].

Therefore, a proper and accurate mathematical model of the robot not only facilitates the design of the advanced control strategies but also possibly realizes affordable robotic solutions for rehabilitation area. In this context, this study presents the kinematical and dynamical modelling approach and the resultant models of a multipurpose upper limb rehabilitation robot, referred to as the Universal Haptic Pantograph (UHP) [29]. The UHP is a pantograph based innovative device actuated by two SEAs (Series Elastic Actuator) whose main characteristic is the reconfigurability of its mechanical structure using lockable/unlockable joints. This feature allows to adapt the structure to the rehabilitation needs of different parts of the upper limb [30].

The article is organized as follows. In Section 2 the UHP rehabilitation robot and the adopted modelling approach are presented. In Section 3, as a first subsystem of UHP, the SEA based drive system and its kinematical and dynamical models are identified. Section 4 describes the identification procedure of the kinematical and dynamical models of the Pantograph which is a subsystem directly contacting users upper limbs. In Section 5, several experimental case studies are presented in order to validate the models. Finally, the most important ideas and conclusions appear in Section 6.

2. Universal Haptic Pantograph and the modelling approach

The Universal Haptic Pantograph (UHP) (Fig. 1) is a rehabilitation robot developed to train impaired upper limbs after a stroke [29]. One of the most important benefits of the UHP is its reconfigurability, which allows to modify its mechanical structure thanks to its lockable / unlockable joints. In this way, for each mechanical configuration, the UHP can execute different types of exercises that focus on certain parts of the upper limb: the shoulder, elbow and wrist [30].

This work focuses in one of the most complete modes, the ARM mode. This mode is used to rehabilitate elbow and shoulder by means of 2 degrees of freedom (DOF) motions that allow arm extension in forward, backward, leftward and rightward directions.

In order to provide this movement, a pantograph-based structure is used to interact with the patient. The Pantograph is actuated by two perpendicular SEAs (Series Elastic Actuator) in order to generate forces in x and y directions as shown in 'SEA based drive system' block in Fig. 1.

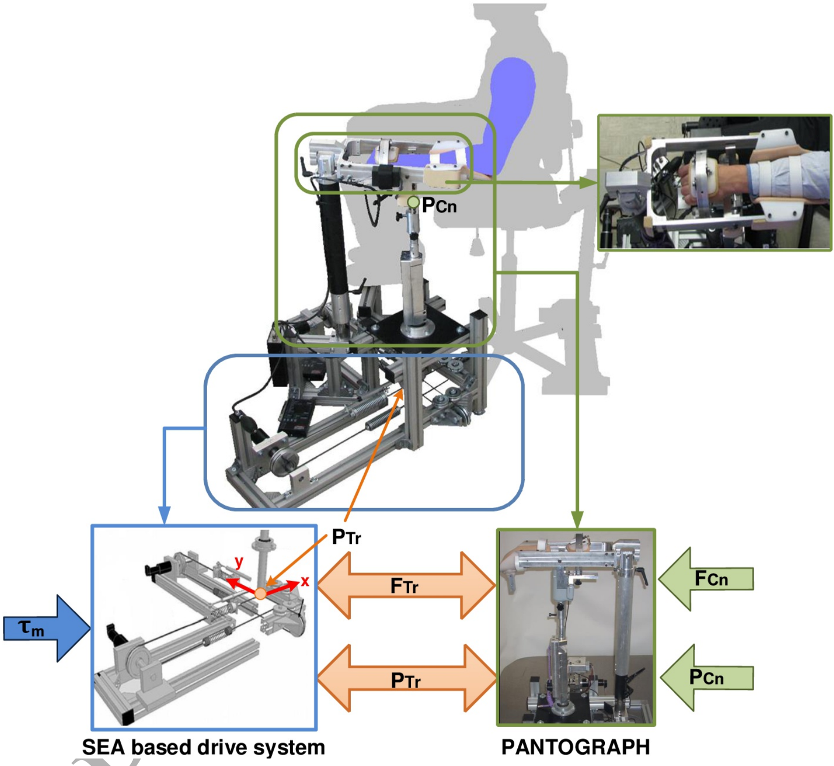

Figure 1: Universal Haptic Pantograph (UHP).

The motion of the UHP results from the forces ($\mathbf{F_{Cn}}$) exerted by the user in the contact point ($\mathbf{P_{Cn}}$) and the torques ($\tau_\mathbf{m}$) exerted by the motors through the SEA based drive system. The two subsystems are connected in the transmission point ($\mathbf{P_{Tr}}$) such that the torque ($\tau_\mathbf{m}$) exerted by the actuators of the drive system and the force ($\mathbf{F_{Cn}}$) and motion ($\mathbf{P_{Cn}}$) applied to the Pantograph by the patient are transmitted bilaterally in the form of force ($\mathbf{F_{Tr}}$) and motion ($\mathbf{P_{Tr}}$) (Fig. 1).

As mentioned previously, a proper mathematical model of the robot is required to implement the robot-patient force interaction controller. Since the model demands position measurements of the drive system for the estimation of the torque ($\tau_{\mathbf{m}}$), the force ($\mathbf{F_{Cn}}$) and motion ($\mathbf{P_{Cn}}$) shown in Fig. 2, the UHP prototype includes two optical encoders and two linear potentiometers to measure the actuators rotation angle ($\mathbf{q_m}$) and the lengths of SEAs upper springs (n_{S_A} and n_{S_B}) respectively.

The inputs and outputs of the model are detailed in Fig. 2. The model of the SEA based drive system is used to compute the actuators torque ($\tau_{\mathbf{m}}$) in the force controller as well as to estimate the force ($\mathbf{F_{Tr}}$) and motion ($\mathbf{P_{Tr}}$) of the transmission point. The Pantograph model, on the other hand, estimates the force ($\mathbf{F_{Cn}}$) and motion ($\mathbf{P_{Cn}}$) applied by the patient. Both models will be detailed in Sections 3 and 4 respectively.

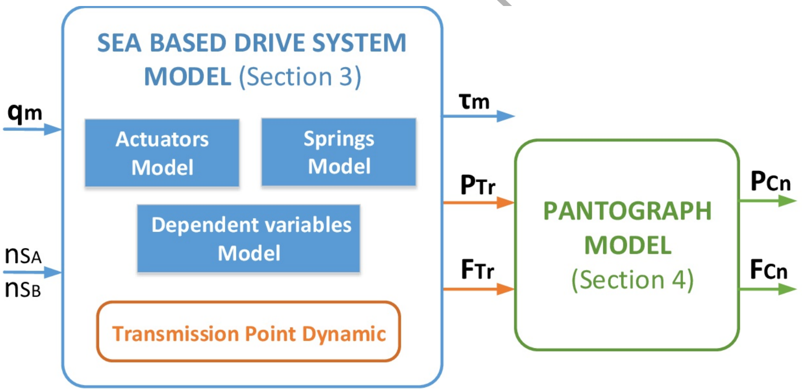

Figure 2: UHP model subsystems.

3. Modelling of SEA based drive system

The UHP drive system is composed of two perpendicular SEAs [29, 31] and each SEA consists of an electrical actuator and a spring that makes the interface between the actuator and the load flexible, thus allows more accurate and stable force control [32]. Due to these advantages, SEAs have been often used in human-robot interaction devices [33].

The SEAs used in the UHP are composed of two Maxon RE40 rotary motors (m_1 and m_2) with integrated encoders, four elastic springs (S_A, S_B, S_C and S_D) and actuated (p_1) and unactuated (p_2) pulleys as shown in Fig. 3. $\mathbf{P_{Tr}}$, a point where SEA based drive system is connected to the Pantograph, is referred to as the transmission point and expressed by $\mathbf{P_{Tr}} = [x_{Tr}\ y_{Tr}\ z_{Tr}]^T$ (Fig. 3).

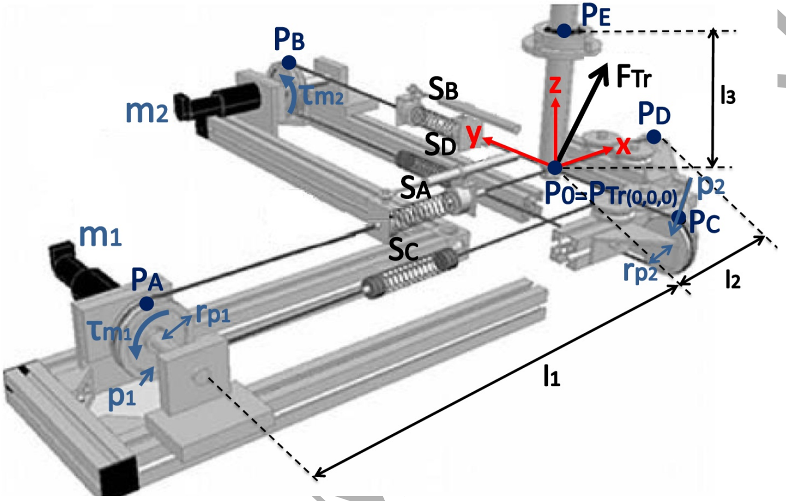

Figure 3: Detailed 3D Structure of SEA based drive system in UHP.

The force and motion transmission from the electric motors (m_1 or m_2) to the springs (S_A and S_C or S_B and S_D) and the transmission point $\mathbf{P_{Tr}}$ is carried out by cables. The SEAs are aligned with x and y axes (Fig. 3). By this configuration, the torque (τ_{m_1}) exerted by motor m_1 is transmitted to springs S_A and S_C and accordingly its force (F_{S_A} and F_{S_C}) are transmitted to the transmission point $\mathbf{P_{Tr}}$, resulting in the movement (x_{Tr}) in the x axis. In a similar way, the y directional motion (y_{Tr}) is generated by the SEA involving motor m_2 and springs S_B and S_D.

The parameters used to define the geometry of the SEA drive system are detailed next. l_1 is the distance from the equilibrium point of the transmission point ($\mathbf{P_0} = \mathbf{P_{Tr}}$ when $x_{Tr} = y_{Tr} = z_{Tr} = 0$) to the center of the actuated pulleys (p_1). l_2 is the distance between $\mathbf{P_0}$ and the center of the unactuated pulleys

(p_2) (Fig. 3). In Fig 5, it can be observed that $\mathbf{l_i}$ is a length vector between $\mathbf{P_i}$ and the transmission point $(\mathbf{P_{Tr}})$ to $i = A; B; C; D$. l_{0_i} is the initial length of the spring S_i. The passive joint variables, $\mathbf{q_{nas}} = [\beta_A\ \beta_B\ \beta_C\ \beta_D\ \delta_A\ \delta_B\ \delta_C\ \delta_D]^T$, are the angles required to describe the direction and orientation of the cables composing the drive system.

The role of the drive system is to exert the appropriate force to the Pantograph such that the transmitted force $(\mathbf{F_{Tr}})$ tracks the desired one. The force $\mathbf{F_{Tr}}$ depends on the variable length of the springs $(\mathbf{n_S} = [n_{S_A}\ n_{S_B}\ n_{S_C}\ n_{S_D}]^T)$, the dependent variables $(\mathbf{q_{nas}} = [\beta_A\ \beta_B\ \beta_C\ \beta_D\ \delta_A\ \delta_B\ \delta_C\ \ \delta_D]^T)$, and the torque exerted by the motors $(\tau_{\mathbf{m}} = [\tau_{m_1}\ \tau_{m_2}]^T)$ (Figs. 3 and 5).

The relationship between the aforementioned variables will be formulated through three steps as highlighted in Fig. 4. First, the kinematical model of elastic components in SEA will be calculated in Section 3.1. Second, motor dynamics will be analyzed to obtain the relationship between their rotation angles $(\mathbf{q_m})$ and the exerted motor torques $(\tau_{\mathbf{m}})$ in Section 3.2. Finally, transmission point dynamics will be identified to calculate the transmission force $(\mathbf{F_{Tr}})$ in Section 3.3.

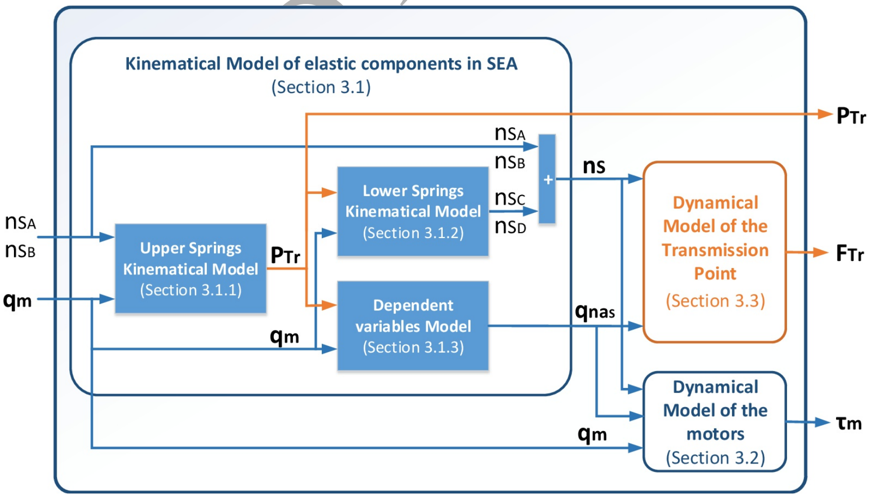

Figure 4: Block diagram of sub-models composing the SEA based drive system.

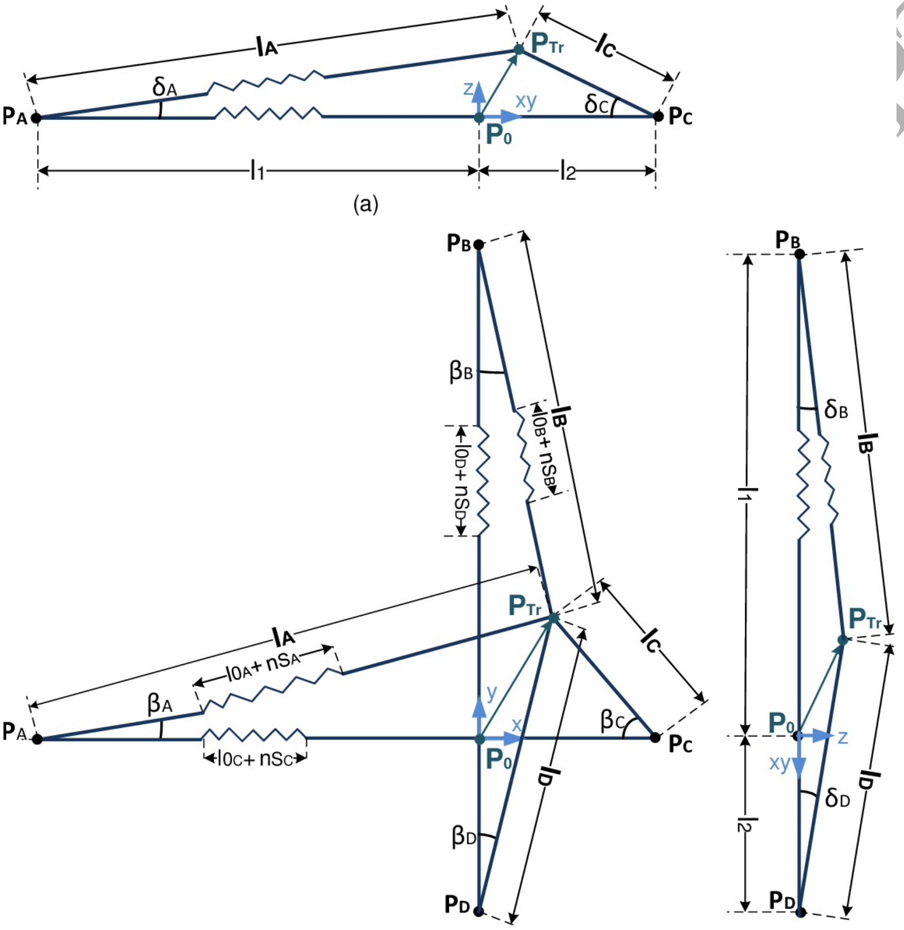

(a)

(b)

(c)

Figure 5: Schematic views of elastic elements and their configuration used in SEAs: (a) the projected view of x directional elastic components of SEAs in xy-z plane, (b) the projected view of x and y directional elastic components in x-y plane, (c) the projected view of y directional elastic components of SEA in xy-z plane.

3.1. Kinematical model of elastic components in SEA

To derive the kinematical model of SEA based drive system, spring variable lengths ($\mathbf{n_S}$) (Sections 3.1.1 and 3.1.2) and the values of the dependent variables ($\mathbf{q_{na_S}}$) (Sections 3.1.3) will be calculated in terms of the rotation angles of the motors ($\mathbf{q_m}$) (Fig. 4).

3.1.1. Upper springs kinematical model

If linear springs are considered, the force exerted by each spring is proportional to the linear deformation, i.e., the variable length of the spring ($\mathbf{n_S}$). In the UHP, springs S_A and S_B are sensorized using linear potentiometers, while springs S_C and S_D are not sensorized.

Figs. 3 and 5 show that n_{S_C} and n_{S_D} depend on the rotation angle of the motors ($\mathbf{q_m}$) and the motion of the transmission point ($\mathbf{P_{Tr}}$). Hence, to obtain n_{S_C} and n_{S_D}, first $\mathbf{P_{Tr}}$ needs to be calculated. To this end, in this section, the $\mathbf{P_{Tr}}$ is formulated in terms of the rotary angles of the motors $\mathbf{q_m}$ and the upper spring lengths n_{S_A} and n_{S_B}.

If stiff and undeformable cables are considered, from Fig. 5, the vectorial equation system that determines the upper cable length vectors ($\mathbf{l_A}$ and $\mathbf{l_B}$) in terms of the transmission motion ($\mathbf{P_{Tr}} = [x_{Tr}\ y_{Tr}\ z_{Tr}]^T$) and the position of $\mathbf{P_A} = [x_A\ 0\ z_A]^T$ and $\mathbf{P_B} = [0\ y_B\ z_B]^T$ is obtained,

$$\begin{aligned}
\mathbf{l_A} + \mathbf{P_A} - \mathbf{P_{Tr}} = \mathbf{0} \rightarrow \mathbf{l_A} &= \begin{bmatrix} x_{Tr} \\ y_{Tr} \\ z_{Tr} \end{bmatrix} - \begin{bmatrix} x_A \\ 0 \\ z_A \end{bmatrix} \\
\mathbf{l_B} + \mathbf{P_B} - \mathbf{P_{Tr}} = \mathbf{0} \rightarrow \mathbf{l_B} &= \begin{bmatrix} x_{Tr} \\ y_{Tr} \\ z_{Tr} \end{bmatrix} - \begin{bmatrix} 0 \\ y_B \\ z_B \end{bmatrix}
\end{aligned} \tag{1}$$

From Eq. 1, the relationship between the upper cable lengths l_A and l_B and the transmission point displacement $\mathbf{P_{Tr}} = [x_{Tr}\ y_{Tr}\ z_{Tr}]^T$ can be formulated by,

$$l_A = |\mathbf{l_A}| = \sqrt{(x_{Tr} - x_A)^2 + y_{Tr}^2 + (z_{Tr} - z_A)^2}$$
$$l_B = |\mathbf{l_B}| = \sqrt{x_{Tr}^2 + (y_{Tr} - y_B)^2 + (z_{Tr} - z_B)^2} \tag{2}$$

On the other hand, from Fig. 5 the relationship between the upper cable length l_A and l_B and the measurable upper spring lengths n_{S_A} and n_{S_B} can be defined in terms of the rotation angle of each motor q_{m_i},

$$n_{S_A} = l_A + (q_{m_1} - \theta_A)\, r_{p_1} - l_1$$
$$n_{S_B} = l_B + (q_{m_2} - \theta_B)\, r_{p_1} - l_1 \tag{3}$$

where l_1 is the distance from the equilibrium point ($\mathbf{P_0}$) to actuated pulley (p_1), r_{p_1} is the radius of actuated pulleys, and the θ_A and θ_B, which are angles depicted in Figs. 6 and 7, are derived as,

$$\theta_A = \arctan\left(\frac{x_A + l_1}{z_A + r_{p_1}}\right)$$
$$\theta_B = \arctan\left(\frac{y_B - l_1}{z_B + r_{p_1}}\right) \tag{4}$$

Therefore, combining Eqs. 2 and 3 yields

$$n_{S_A} - q_{m_1}\ r_{p_1} = \sqrt{(x_{Tr} - x_A)^2 + y_{Tr}^2 + (z_{Tr} - z_A)^2} - \theta_A\ r_{p_1} - l_1$$
$$n_{S_B} - q_{m_2}\ r_{p_1} = \sqrt{x_{Tr}^2 + (y_B - y_{Tr})^2 + (z_{Tr} - z_B)^2} - \theta_B\ r_{p_1} - l_1 \tag{5}$$

In order to solve Eq. 5, the position vectors of points $\mathbf{P_A}$ ($[x_A\ 0\ z_A]^T$) and $\mathbf{P_B}$ ($[0\ y_B\ z_B]^T$) are required. Applying the Pythagorean theorem to the actuated pulley p_1 in the xz plane (Fig. 6) leads to

$$(x_A + l_1)^2 + (z_A + r_{p_1})^2 = r_{p_1}^2 \tag{6}$$

On the other hand, vector $\mathbf{r_1}$ and the xz plane projection of $\mathbf{l_A}$ ($\mathbf{l_{A_{xz}}}$) are normal, that is,

$$\mathbf{r_1} \cdot \mathbf{l_{A_{xz}}} = \mathbf{0} \rightarrow (x_A + l_1)(x_{Tr} - x_A) + (z_A + r_{p_1})(z_{Tr} - z_A) = 0 \tag{7}$$

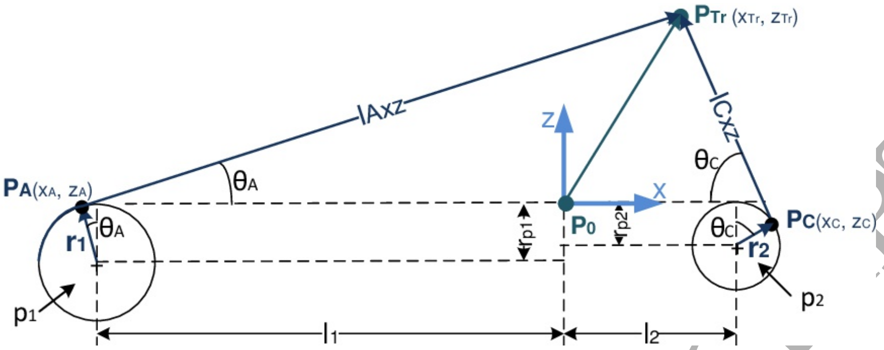

Figure 6: Relation between $\mathbf{P_i}$ ($i = A$ and C) and kinematical parameters of the x-directional SEA in Fig. 5.

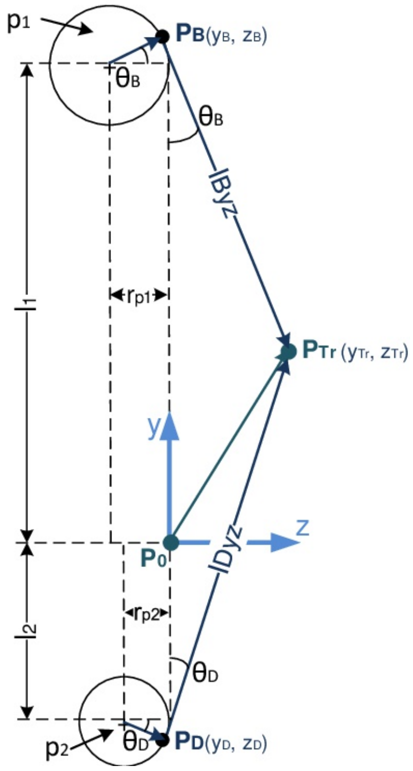

Figure 7: Relation between $\mathbf{P_i}$ ($i = B$ and D) and kinematical parameters of the y-directional SEA in Fig. 5..

Performing the same process to point $\mathbf{P_B}$ (Fig. 7),

$$\begin{aligned} (y_B - l_1)^2 + (z_B + r_{p_1})^2 &= r_{p_1}^2 \\ (y_B - l_1)(y_{Tr} - y_B) + (z_B + r_{p_1})(z_{Tr} - z_B) &= 0 \end{aligned} \tag{8}$$

Combining Eqs. 5 to 8 leads to two equations that relate the transmission point ($\mathbf{P_{Tr}}$) and the measurable variables ($\mathbf{q_m}$, n_{S_A} and n_{S_B}). However, as $\mathbf{P_{Tr}}$ has three variables (x_{Tr}, y_{Tr} and z_{Tr}), a third equation is required to solve the $\mathbf{P_{Tr}}$. The third equation can be obtained by analyzing the motion of the Pantograph actuated bar. The actuated bar presents a spherical joint $\mathbf{P_E}$ with respect to the Fixed structure (Fig. 3). Thus, the motion of $\mathbf{P_{Tr}}$ is constrained to the surface of a sphere of radius l_3,

$$x_{Tr}^2 + y_{Tr}^2 + (l_3 - z_{Tr})^2 = l_3^2 \tag{9}$$

which is the third equation to solve the $\mathbf{P_{Tr}}$.

3.1.2. Lower springs kinematical model

After solving the $\mathbf{P_{Tr}}$, the estimation of lengths n_{S_C} and n_{S_D} based on the measurable variables is required according to the procedure presented in Fig. 4. For that purpose, a similar procedure as that employed in the previous section is applied. From Fig. 5,

$$\begin{aligned} \mathbf{P_C} + \mathbf{l_C} - \mathbf{P_{Tr}} = \mathbf{0} \rightarrow \mathbf{l_C} &= \begin{bmatrix} x_{Tr} \\ y_{Tr} \\ z_{Tr} \end{bmatrix} - \begin{bmatrix} x_C \\ 0 \\ z_C \end{bmatrix} \\ \mathbf{P_D} + \mathbf{l_D} - \mathbf{P_{Tr}} = \mathbf{0} \rightarrow \mathbf{l_D} &= \begin{bmatrix} x_{Tr} \\ y_{Tr} \\ z_{Tr} \end{bmatrix} + \begin{bmatrix} 0 \\ y_D \\ z_D \end{bmatrix} \end{aligned} \tag{10}$$

where $[x_C\ 0\ z_C]^T$ and $[0\ y_D\ z_D]^T$ are positions of $\mathbf{P_C}$ and $\mathbf{P_D}$ respectively.

The norm associated to each vector is,

$$\begin{aligned} l_C = |\mathbf{l_C}| &= \sqrt{(x_{Tr} - x_C)^2 + y_{Tr}^2 + (z_{Tr} - z_C)^2} \\ l_D = |\mathbf{l_D}| &= \sqrt{x_{Tr}^2 + (y_{Tr} + y_D)^2 + (z_{Tr} + z_D)^2} \end{aligned} \tag{11}$$

To determine the position of the point $\mathbf{P_C}$, the Pythagorean theorem is applied to the unactuated pulley p_2 (Fig. 6), which is contained in the xz plane,

$$(x_C - l_2)^2 + (z_C + r_{p_2})^2 = r_{p_2}^2 \tag{12}$$

where l_2 is the distance from the equilibrium point ($\mathbf{P_0}$) to the unactuated pulleys (p_2) and r_{p_2} is the pulleys radius.

On the other hand, vector $\mathbf{r_2}$ and the xz plane projection of $\mathbf{l_C}$ ($\mathbf{l_{C_{xz}}}$) are normal (Fig. 6), that is,

$$\mathbf{r_2} \cdot \mathbf{l_{C_{xz}}} = \mathbf{0} \rightarrow (x_C - l_2)(x_{Tr} - x_C) + (z_C + r_{p_2})(z_{Tr} - z_C) = 0 \tag{13}$$

Performing the same process to point $\mathbf{P_D}$ (Fig. 7),

$$\begin{aligned} (y_D + l_2)^2 + (z_D + r_{p_2})^2 &= r_{p_2}^2 \\ (y_D + l_2)(y_{Tr} - y_D) + (z_D + r_{p_2})(z_{Tr} - z_D) &= 0 \end{aligned} \tag{14}$$

Therefore, by solving Eqs. 12 - 14 and inserting $\mathbf{P_C} = [x_C \ 0 \ z_C]^T$ and $\mathbf{P_D} = [0 \ y_D \ z_D]^T$ in Eq. 11, l_C and l_D are calculated.

So, the variable length of unsensorized springs are (Fig. 5),

$$\begin{aligned} n_{S_C} &= l_C - q_{m_1} \ r_{p_1} + \theta_C \ r_{p_2} - l_2 \\ n_{S_D} &= l_D - q_{m_2} \ r_{p_1} + \theta_D \ r_{p_2} - l_2 \end{aligned} \tag{15}$$

where from Figs. 6 and 7,

$$\begin{aligned} \theta_C &= \arctan\left(\frac{x_C - l_2}{z_C + r_{p_2}}\right) \\ \theta_D &= \arctan\left(\frac{y_D + l_2}{z_D + r_{p_2}}\right) \end{aligned} \tag{16}$$

3.1.3. Determination of dependent variables in the model

As described in Fig. 4, after formulating the springs variable length ($\mathbf{n_S}$) and the position of the $\mathbf{P_{Tr}}$, it is required to compute the dependent variables ($\mathbf{q_{na_S}} = [\beta_A \ \beta_B \ \beta_C \ \beta_D \ \delta_A \ \delta_B \ \delta_C \ \delta_D]^T$) to complete kinematical model of the drive system.

As it can be seen in Fig. 5, β_i is the angle between axes x and y, and δ_i is the angle between axis z and plane xy that defines the direction of l_i to $i = A; B; C; D$. By applying trigonometry, the following relationships are obtained:

$$\begin{aligned}
\beta_A &= \arctan\left(\frac{y_{Tr}}{x_{Tr} - x_A}\right) \\
\beta_B &= \arctan\left(\frac{x_{Tr}}{y_B - y_{Tr}}\right) \\
\beta_C &= \arctan\left(\frac{y_{Tr}}{x_C - x_{Tr}}\right) \\
\beta_D &= \arctan\left(\frac{x_{Tr}}{y_{Tr} - y_D}\right)
\end{aligned} \tag{17}$$

$$\begin{aligned}
\delta_A &= \arctan\left(\frac{z_{Tr} - z_A}{\sqrt{(x_{Tr} - x_A)^2 + y_{Tr}^2}}\right) \\
\delta_B &= \arctan\left(\frac{z_{Tr} - z_B}{\sqrt{x_{Tr}^2 + (y_B - y_{Tr})^2}}\right) \\
\delta_C &= \arctan\left(\frac{z_{Tr} - z_C}{\sqrt{(x_C - x_{Tr})^2 + y_{Tr}^2}}\right) \\
\delta_D &= \arctan\left(\frac{z_{Tr} - z_D}{\sqrt{x_{Tr}^2 + (y_{Tr} - y_D)^2}}\right)
\end{aligned} \tag{18}$$

3.2. Dynamical model of the actuators

Once the variable lengths ($\mathbf{n_S}$) of the springs and the dependent variables ($\mathbf{q_{na_S}}$) are calculated, the dynamical model of the motor can be obtained (Fig. 4).

The actuation torque exerted by each motor $j = 1; 2$ (τ_{m_j}) is calculated as,

$$\tau_{m_j} - \tau_{S_j} = I_{m_j}\ddot{q}_{m_j} + B_{m_j}\dot{q}_{m_j} + Fc_j \tanh(\beta_j \dot{q}_{m_j}) \tag{19}$$

where I_{m_j} is the inertia, B_{m_j} the torsional viscous friction coefficient and F_{c_j} and β_j the Coulomb friction [34]. $\tau_{S_1} = \tau_{S_A} + \tau_{S_C}$ and $\tau_{S_2} = \tau_{S_B} + \tau_{S_D}$ define the equivalent torques exerted by the springs in each motor $j = 1; 2$. This torque is calculated by multiplying the force exerted by each spring ($\mathbf{F^m_{S_i}}$) by the radius of the actuated pulley (r_{p_1}) (Figs. 8 and 9). As motor m_1 is contained in plane xz and motor m_2 in plane yz,

$$\begin{aligned}\tau_{S_1} &= \tau_{S_A} + \tau_{S_C} = \left|\mathbf{F^m_{S_{A_{xz}}}}\right| r_{p_1} + \left|\mathbf{F^m_{S_{C_{xz}}}}\right| r_{p_1} \\ \tau_{S_2} &= \tau_{S_B} + \tau_{S_D} = \left|\mathbf{F^m_{S_{B_{yz}}}}\right| r_{p_1} + \left|\mathbf{F^m_{S_{D_{yz}}}}\right| r_{p_1}\end{aligned} \tag{20}$$

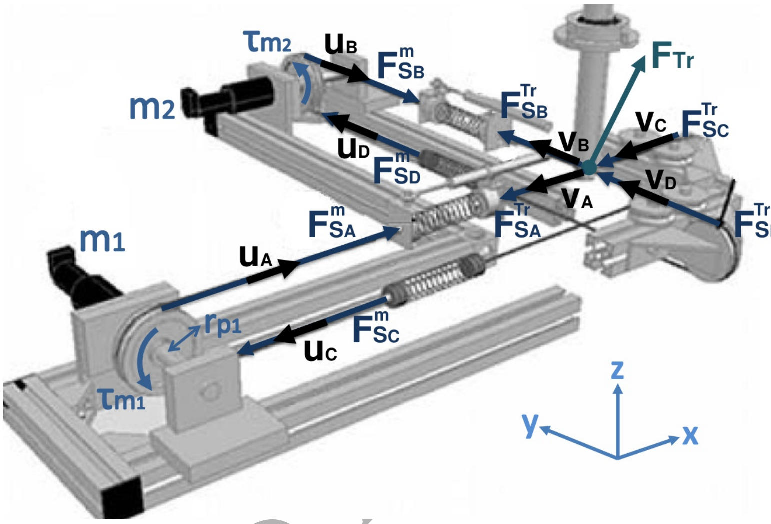

Figure 8: Representation of forces and torques resulting from the springs and motors in SEA based drive system.

On the other hand, the magnitude of each spring force (F_{S_i}) depends on its variable length (n_{S_i}) and its constant (k_{S_i}), while its direction ($\mathbf{u_i}$) depends on the passive variables ($\mathbf{q_{nas}}$),

$$\mathbf{F^m_{S_i}}(n_{S_i}, \mathbf{q_{nas}}) = F_{S_i}\ \mathbf{u_i} = k_{S_i}\ n_{S_i}\ \mathbf{u_i} \tag{21}$$

where the unitary force direction vectors $\mathbf{u_i}$ are (Figs. 5 and 9),

$$\begin{aligned}\mathbf{u_A} &= [\ \cos\beta_A\cos\delta_A \quad \sin\beta_A\cos\delta_A \quad \sin\delta_A\ ]^T \\ \mathbf{u_B} &= [\ \sin\beta_B\cos\delta_B \quad -\cos\beta_B\cos\delta_B \quad \sin\delta_B\ ]^T \\ \mathbf{u_C} &= [\ -1 \quad 0 \quad 0\ ]^T \\ \mathbf{u_D} &= [\ 0 \quad 1 \quad 0\ ]^T\end{aligned} \tag{22}$$

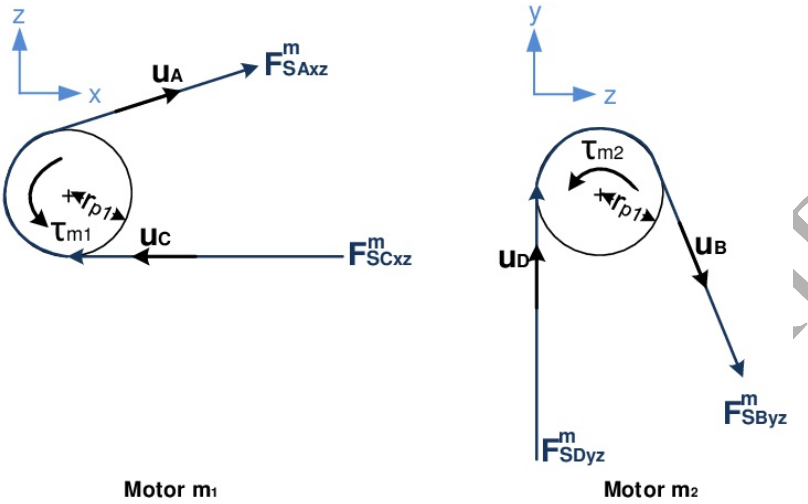

Figure 9: Torque exerted by each motor (τ_{m_j}, $j = 1; 2$).

So, the torques exerted by the springs in each motor are,

$$\tau_{S_1} = \tau_{S_A} + \tau_{S_C} = k_{S_A} n_{S_A} r_{p_1} \sqrt{\cos^2\beta_A \cos^2\delta_A + \sin^2\delta_A} + k_{S_C} n_{S_C} r_{p_1}$$
$$\tau_{S_2} = \tau_{S_B} + \tau_{S_D} = k_{S_B} n_{S_B} r_{p_1} \sqrt{\cos^2\beta_B \cos^2\delta_B + \sin^2\delta_B} + k_{S_D} n_{S_D} r_{p_1} \quad (23)$$

3.3. Dynamical model of the drive system: dynamics of Transmission Point

As a final step in modelling of SEA based drive system, dynamics of the transmission point is identified (Fig. 4). The transmission point $\mathbf{P_{Tr}}$ defines the contact point between the Pantograph and the drive system. As the drive system is based on a motor-spring actuation, the exerted force ($\mathbf{F_{Tr}}$) is calculated based on the spring forces that are transmitted through the cables ($\mathbf{F^{Tr}_{S_i}}$) (Figs. 8 and 10),

$$\mathbf{F_{Tr}} = \sum_{i=A}^{D} \mathbf{F^{Tr}_{S_i}} = \mathbf{F^{Tr}_{S_A}} + \mathbf{F^{Tr}_{S_B}} + \mathbf{F^{Tr}_{S_C}} + \mathbf{F^{Tr}_{S_D}} \quad (24)$$

The magnitude of each spring force (F_{S_i}) depends on its variable length (n_{S_i}) and its constant (k_{S_i}), while its direction ($\mathbf{v_i}$) depends on the passive variables ($\mathbf{q_{na_S}}$),

$$\mathbf{F^{Tr}_{S_i}}(n_{S_i}, \mathbf{q_{na_S}}) = k_{S_i}\ n_{S_i}\ \mathbf{v_i} \quad (25)$$

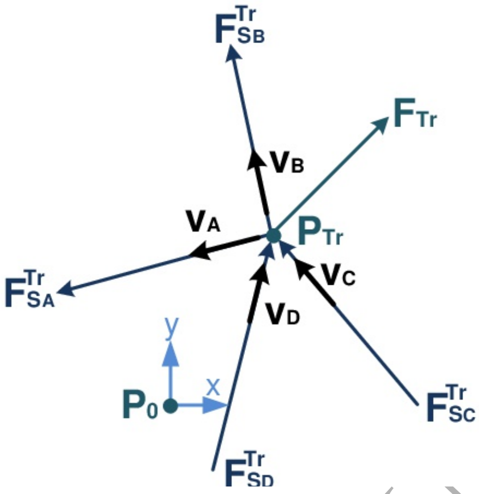

Figure 10: Resultant force ($\mathbf{F_{Tr}}$) at Transmission point ($\mathbf{P_{Tr}}$).

where $\mathbf{v_i}$ is the unitary direction vector of $\mathbf{l_i}$ to $i = A; B; C; D$, which depends on $\mathbf{q_{nas}} = [\beta_A\ \beta_B\ \beta_C\ \beta_D\ \delta_A\ \delta_B\ \delta_C\ \delta_D]^T$ (Figs. 5 and 10),

$$\begin{aligned}
\mathbf{v_A} &= [\,-\cos\beta_A\cos\delta_A \quad -\sin\beta_A\cos\delta_A \quad -\sin\delta_A\,]^T\\
\mathbf{v_B} &= [\,-\sin\beta_B\cos\delta_B \quad \cos\beta_B\cos\delta_B \quad -\sin\delta_B\,]^T\\
\mathbf{v_C} &= [\,-\cos\beta_C\cos\delta_C \quad \sin\beta_C\cos\delta_C \quad \sin\delta_C\,]^T\\
\mathbf{v_D} &= [\,\sin\beta_D\cos\delta_D \quad \cos\beta_D\cos\delta_D \quad \sin\delta_D\,]^T
\end{aligned} \tag{26}$$

So, the transmission force ($\mathbf{F_{Tr}}$) in terms of the variable length ($\mathbf{n_S}$) of the springs and the dependent variables ($\mathbf{q_{nas}}$) is given by,

$$\begin{aligned}
\mathbf{F_{Tr}} &= k_{S_A}n_{S_A}\begin{bmatrix}-\cos\beta_A\cos\delta_A\\ -\sin\beta_A\cos\delta_A\\ -\sin\delta_A\end{bmatrix} + k_{S_B}n_{S_B}\begin{bmatrix}-\sin\beta_B\cos\delta_B\\ \cos\beta_B\cos\delta_B\\ -\sin\delta_B\end{bmatrix}\\
&+ k_{S_C}n_{S_C}\begin{bmatrix}-\cos\beta_C\cos\delta_C\\ \sin\beta_C\cos\delta_C\\ \sin\delta_C\end{bmatrix} + k_{S_D}n_{S_D}\begin{bmatrix}\sin\beta_D\cos\delta_D\\ \cos\beta_D\cos\delta_D\\ \sin\delta_D\end{bmatrix}
\end{aligned} \tag{27}$$

4. Modelling of Pantograph structure

The Pantograph is the part of the UHP rehabilitation robot which interacts with the patient. It is composed of three mobile bars (actuated, transverse and parallel) and a fixed structure [30] (Fig. 11). Moreover, these bars can be represented by five mobile elements ($\mathbf{E_1}$, $\mathbf{E_2}$, $\mathbf{E_3}$, $\mathbf{E_4}$ and $\mathbf{E_5}$) and five joints ($\mathbf{P_E}$, $\mathbf{P_F}$, $\mathbf{P_G}$, $\mathbf{P_H}$ and $\mathbf{P_I}$), where joints $\mathbf{P_F}$, $\mathbf{P_H}$ and $\mathbf{P_I}$ are lockable/unlockable. This mechanical structure allows 2 DoFs motion, depending on the combination of joints $\mathbf{P_F}$, $\mathbf{P_H}$ and $\mathbf{P_I}$.

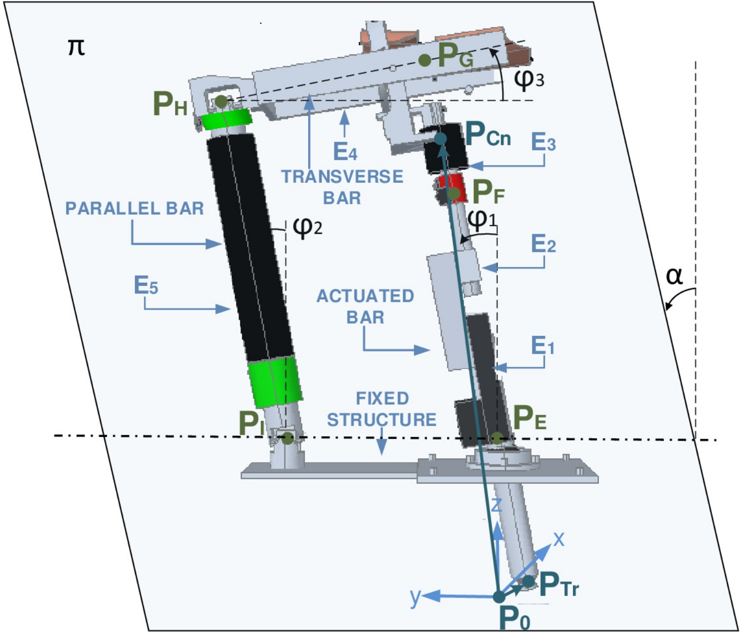

Figure 11: Pantograph in ARM mode.

In ARM mode, as the joint $\mathbf{P_F}$ is locked, relative motion between elements $\mathbf{E_2}$ and $\mathbf{E_3}$ does not happen. Furthermore, revolute joint $\mathbf{P_H}$ and universal joint $\mathbf{P_I}$ are unlocked, in order to allow the motion of the parallel and transverse bars. As a result, a four-bar mechanism structure is defined, where all the bars are always contained in plane π while allowing rotation (α) about y axis (Fig. 11). Similarly, the four-bar mechanism allows motion in the direction of the y axis of π plane, which is defined by the variation of the angles of the actuated (φ_1), parallel (φ_2) and transverse (φ_3) bars with respect to the xz plane.

Therefore, when the drive system applies force at the lower end of the actuated bar ($\mathbf{P_{Tr}}$), this generates movement of both parallel and transverse bars and consequently moves the patients arm attached to Pantograph. The resulting motion in ARM mode is 2 DoFs in x and y directions.

Moreover, thanks to the slider that allows relative translation between elements $\mathbf{E_1}$ and $\mathbf{E_2}$, the actuated bar length can vary. In this way, the transverse bar inclination can be modified to achieve an ergonomical position for the patient (Fig. 11). During the execution of the training exercise, the variable length d_1 is locked in a known position to prevent undesirable changes in its length for the safety(Fig. 12).

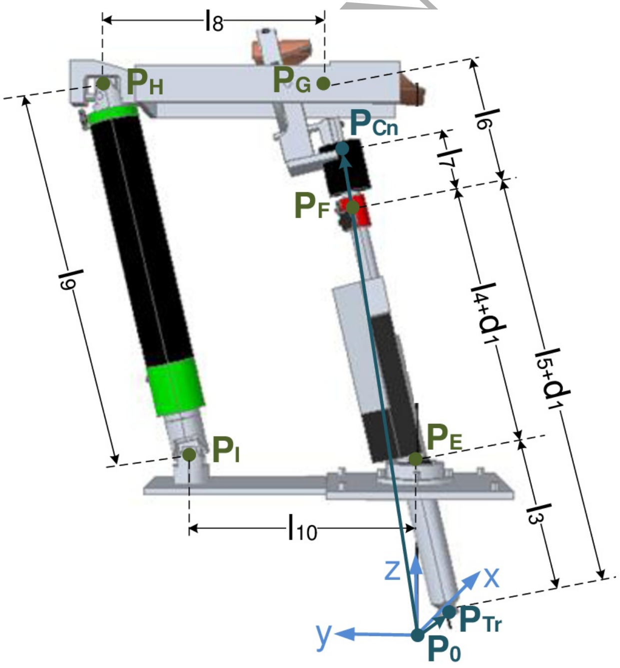

Figure 12: Representation of parameters describing the Pantograph configuration.

In the particular case where the variable length d_1 is zero (Fig. 12), the parallel bar and the actuated bar have the same length. Hence, the structure is a regular four-bar mechanism, in which both pairs of bars, parallel and actuated and transverse and fixed are always parallel ($\varphi_1 = \varphi_2$, $\varphi_3 = 0$).

The equilibrium position of the UHP is achieved when the actuated bar is in vertical position ($\varphi_1 = 0$ and $\alpha = 0$), defining the origin of the base reference frame $\mathbf{P_0} = \mathbf{P_{Tr}}$ ($x_{Tr} = y_{Tr} = z_{Tr} = 0$).

On the other hand, the rest of the parameters that are used to define the geometry of the Pantograph are detailed in Fig. 12.

With the aim of identifying the relationship between the contact ($\mathbf{P_{Cn}}$) and transmission ($\mathbf{P_{Tr}}$) points, the kinematical (Section 4.1) and dynamical (Section 4.2) models of the Pantograph in ARM mode are derived (Fig. 2).

4.1. Kinematical model

First, the Pantograph kinematical model, that relates the motion of the transmission point $\mathbf{P_{Tr}} = [x_{Tr}\ y_{Tr}\ z_{Tr}]^T$, and the contact point position $\mathbf{P_{Cn}} = [x_{Cn}\ y_{Cn}\ z_{Cn}]^T$ are calculated based on the kinematical loop equation (Fig. 12),

$$\mathbf{P_{Tr}} + \mathbf{l_5} + \mathbf{d_1} + \mathbf{l_7} - \mathbf{P_{Cn}} = \mathbf{0} \tag{28}$$

Solving for $\mathbf{P_{Cn}}$,

$$\begin{aligned}\begin{bmatrix} x_{Cn} \\ y_{Cn} \\ z_{Cn} \end{bmatrix} &= \begin{bmatrix} x_{Tr} \\ y_{Tr} \\ z_{Tr} \end{bmatrix} + \frac{l_5 + d_1 + l_7}{l_3} \begin{bmatrix} -x_{Tr} \\ -y_{Tr} \\ l_3 - z_{Tr} \end{bmatrix} \\ &= \frac{-l_4 - d_1 - l_7}{l_3} \begin{bmatrix} x_{Tr} \\ y_{Tr} \\ z_{Tr} \end{bmatrix} + \begin{bmatrix} 0 \\ 0 \\ l_5 + d_1 + l_7 \end{bmatrix}\end{aligned} \tag{29}$$

Eq. 29 relates the input ($\mathbf{P_{Tr}}$) and output ($\mathbf{P_{Cn}}$) motion, but in order to fully define the motion of the Pantograph, the position of point $\mathbf{P_H}$ must be calculated. For this purpose, a geometrical approach based on the intersection of circumferences is used.

In ARM mode, the bars composing the Pantograph are always contained in the π plane, which can rotate α around y axis (Fig. 11). Hence, considering that the Pantograph behaves as a four-bar mechanism, its kinematics can be calculated by defining two circumferences of center in joints $\mathbf{P_G}$ and $\mathbf{P_I}$, and constant radius l_8 and l_9, respectively (Fig. 13). To calculate the intersection, $\mathbf{P_H}$, the coordinates of $\mathbf{P_G}$ and $\mathbf{P_I}$ have to be projected to the plane. To perform this projection the reference system is moved to point $\mathbf{P_E}$ and the axes y^π and w^π are taken as coordinates, where $y^\pi = y$ and $w^\pi = \sqrt{x^2 + (l_3 - z)^2}$.

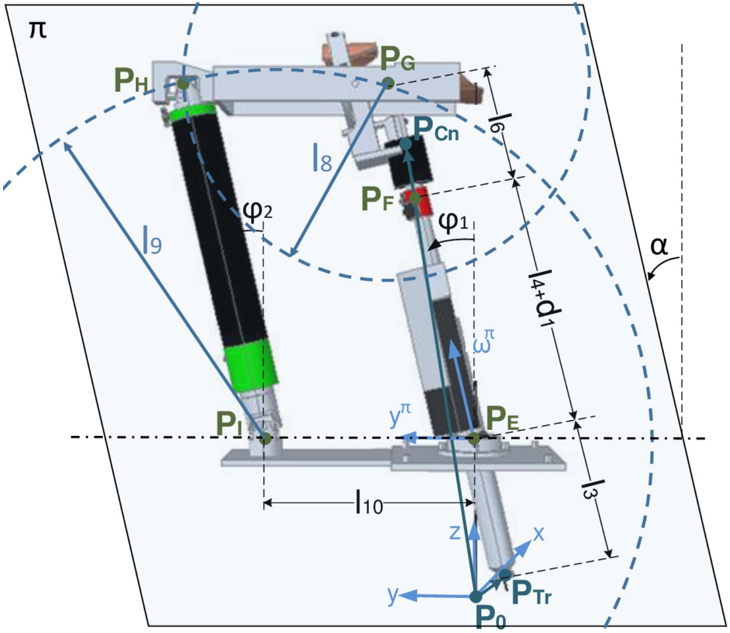

Figure 13: Pantograph projection on the plane π.

The position of the circumferences center ($\mathbf{P_G}$ and $\mathbf{P_I}$) in the reference system of the UHP (x, y, z) are (Fig. 13),

$$\mathbf{P_G} \quad = \quad \mathbf{P_{Tr}} + \mathbf{l_3} + \mathbf{l_4} + \mathbf{d_1} + \mathbf{l_6} = \frac{l_4 + d_1 + l_6}{l_3} \begin{bmatrix} -x_{Tr} \\ -y_{Tr} \\ -z_{Tr} + l_3 \end{bmatrix} + \begin{bmatrix} 0 \\ 0 \\ l_3 \end{bmatrix}$$

$$\mathbf{P_I} \quad = \quad \mathbf{P_{Tr}} + \mathbf{l_3} - \mathbf{l_{10}} = \begin{bmatrix} 0 \\ l_{10} \\ l_3 \end{bmatrix} \tag{30}$$

So, their projection on the plane π ($\mathbf{P_G}^{\pi}$ and $\mathbf{P_I}^{\pi}$),

$$\begin{aligned} \mathbf{P_G}^{\pi} &= \frac{(l_4 + d_1 + l_6)}{l_3} \begin{bmatrix} -y_{Tr} \\ \sqrt{x_{Tr}^2 + (l_3 - z_{Tr})^2} \end{bmatrix} \\ \mathbf{P_I}^{\pi} &= \begin{bmatrix} l_{10} \\ 0 \end{bmatrix} \end{aligned} \tag{31}$$

Therefore, the circumferences, defined in the π plane,

$$\begin{aligned} \left(y_H^{\pi} + \frac{l_4 + d_1 + l_6}{l_3} y_{Tr} \right)^2 + \left(w_H^{\pi} - \frac{l_4 + d_1 + l_6}{l_3} \sqrt{x_{Tr}^2 + (l_3 - z_{Tr})^2} \right)^2 &= l_8^2 \\ (y_H^{\pi} - l_{10})^2 + (w_H^{\pi})^2 &= l_9^2 \end{aligned} \tag{32}$$

Solving the Eq. 32, the intersection point $\mathbf{P_H}^{\pi}$ defined in the π plane coordinate system is obtained. So, its value in the reference system of the UHP (x, y, z) is,

$$\begin{aligned} x_H &= w_H^{\pi} \sin\alpha \\ y_H &= y_H^{\pi} \\ z_H &= w_H^{\pi} \cos\alpha + l_3 \end{aligned} \tag{33}$$

where the angle α is the inclination angle of plane π with respect to xz plane, and is defined as,

$$\alpha = \arctan\left(\frac{x_E - x_{Tr}}{z_E - z_{Tr}} \right) = \arctan\left(\frac{-x_{Tr}}{l_3 - z_{Tr}} \right) \tag{34}$$

Once the α is calculated , the rest of the passives variables that define the kinematical model of the Pantograph ($\mathbf{q_{na_A}} = [\alpha \ \varphi_1 \ \varphi_2 \ \varphi_3]^T$) can be obtained knowing that $y^{\pi} = y$ and $w^{\pi} = \sqrt{x^2 + (l_3 - z)^2}$ (Figs. 11 and 13),

$$\begin{aligned} \varphi_1 &= \arctan\left(\frac{y_E^{\pi} - y_{Tr}^{\pi}}{w_E^{\pi} - w_{Tr}^{\pi}} \right) = \arctan\left(\frac{y_{Tr}^{\pi}}{w_{Tr}^{\pi}} \right) \\ &= \arctan\left(\frac{y_{Tr}}{\sqrt{x_{Tr}^2 + (l_3 - z_{Tr})^2}} \right) \end{aligned} \tag{35}$$

$$\begin{aligned} \varphi_2 &= \arctan\left(\frac{y_H^\pi - y_I^\pi}{w_H^\pi - w_I^\pi}\right) = \arctan\left(\frac{y_H^\pi + l_{10}}{w_H^\pi}\right) \\ &= \arctan\left(\frac{y_H + l_{10}}{\sqrt{x_H^2 + (l_3 - z_H)^2}}\right) \end{aligned} \tag{36}$$

$$\varphi_3 = \arctan\left(\frac{w_G^\pi - w_H^\pi}{y_G^\pi - y_H^\pi}\right) \tag{37}$$

where y_G^π and w_G^π are defined in Eq. 31, so,

$$\varphi_3 = \arctan\left(\frac{l_3 w_H - l_4 - d_1 - l_6\sqrt{x_{Tr}^2 + (l_3 - z_{Tr})^2}}{l_3 y_H + l_4 + d_1 + l_6 y_{Tr}}\right) \tag{38}$$

In the particular case where $d_1 = 0$, the actuated and the parallel bars will have an equal length, so w_H^π=w_G^π, φ_3=0 and $\varphi_1 = \varphi_2$.

Once the position problem is defined, the speed problem of the Pantograph can be completely defined by calculating the Jacobian matrices relating the time derivatives of the output variables ($\mathbf{\dot{P}_{Cn}}$) and passives variables ($\mathbf{\dot{q}_{na_A}}$) with the time derivative of the input variables ($\mathbf{\dot{P}_{Tr}}$).

Hence, derivating Eq.29, the input-output Jacobian can be calculated,

$$\mathbf{\dot{P}_{Cn}} = \underbrace{\mathbf{J_x}}_{3x3}\mathbf{\dot{P}_{Tr}} \tag{39}$$

Similarly, inserting $\mathbf{P_H}$ value and taking the time derivative in Eqs. 34 - 37,

$$\begin{aligned} \dot{\alpha} &= \underbrace{\mathbf{J}_\alpha}_{1x3}\mathbf{\dot{P}_{Tr}} \\ \dot{\varphi}_1 &= \underbrace{\mathbf{J}_{\varphi_1}}_{1x3}\mathbf{\dot{P}_{Tr}} \\ \dot{\varphi}_2 &= \underbrace{\mathbf{J}_{\varphi_2}}_{1x3}\mathbf{\dot{P}_{Tr}} \\ \dot{\varphi}_3 &= \underbrace{\mathbf{J}_{\varphi_3}}_{1x3}\mathbf{\dot{P}_{Tr}} \end{aligned} \tag{40}$$

Combining Eqs. 39 and 40,

$$\dot{\mathbf{q}}_{\mathbf{na_A}} = \begin{bmatrix} \dot{\alpha} \\ \dot{\varphi}_1 \\ \dot{\varphi}_2 \\ \dot{\varphi}_3 \end{bmatrix} = \begin{bmatrix} \mathbf{J}_{\alpha} \\ \mathbf{J}_{\varphi_1} \\ \mathbf{J}_{\varphi_2} \\ \mathbf{J}_{\varphi_3} \end{bmatrix} \dot{\mathbf{P}}_{\mathbf{Tr}} = \mathbf{J}_{\mathbf{q_{na_A}}} \dot{\mathbf{P}}_{\mathbf{Tr}} = \mathbf{J}_{\mathbf{q_{na_A}}} \mathbf{J_x}^{-1} \dot{\mathbf{P}}_{\mathbf{Cn}} \tag{41}$$

4.2. Dynamical model: dynamics of Transmission point

The dynamical model of the Pantograph is used to determine the relationship between the transmission force from the SEA ($\mathbf{F_{Tr}}$) and the contact force from the patient ($\mathbf{F_{Cn}}$) depending on the transmission motion ($\mathbf{P_{Tr}}$). For this purpose, the Lagrangian formulation is used [35].

In ARM mode the Pantograph is composed by five elements ($\mathbf{E_1}$, $\mathbf{E_2}$, $\mathbf{E_3}$, $\mathbf{E_4}$ and $\mathbf{E_5}$, where $\mathbf{E_1}$, $\mathbf{E_2}$, $\mathbf{E_3}$ have the same motion due to the lockable joints $\mathbf{P_F}$) (Fig. 14).

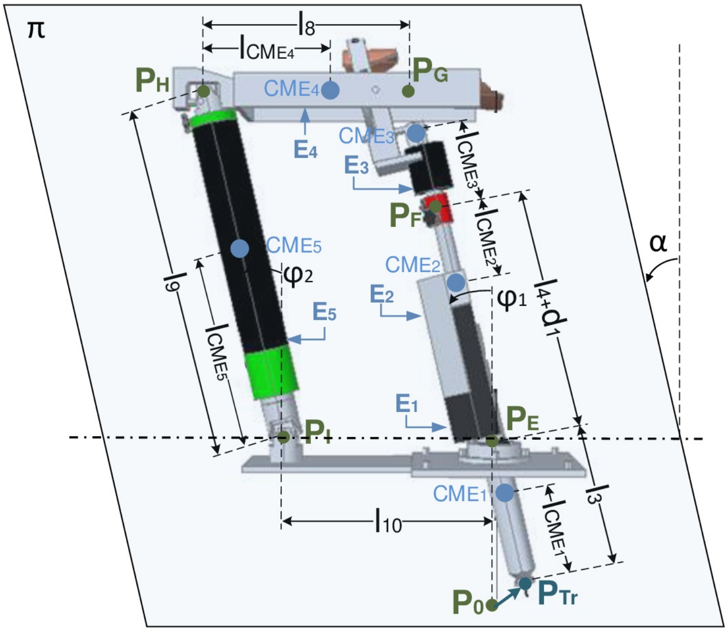

Figure 14: Position of center of mass of Pantograph segments.

Therefore, the Langrangian function can be defined as,

$$\mathbf{L} = \mathbf{K_{E_1}} + \mathbf{K_{E_2}} + \mathbf{K_{E_3}} + \mathbf{K_{E_4}} + \mathbf{K_{E_5}} - (\mathbf{U_{E_1}} + \mathbf{U_{E_2}} + \mathbf{U_{E_3}} + \mathbf{U_{E_4}} + \mathbf{U_{E_5}}) \tag{42}$$

where $\mathbf{K_{E_i}}$ and $\mathbf{U_{E_i}}$ are kinetic and potential energies of each element, defined as,

$$\mathbf{K_{E_i}} = \frac{1}{2}\, m_{E_i}\, \mathbf{v_{CM_{E_i}}}^T\, \mathbf{v_{CM_{E_i}}} + \frac{1}{2}\, \omega_{\mathbf{CM_{E_i}}}{}^T\, \mathbf{I_{E_i}}\, \omega_{\mathbf{CM_{E_i}}} \tag{43}$$

$$\mathbf{U_{E_i}} = m_{E_i}\, g\, h_{CM_{E_i}} \tag{44}$$

where m_{E_i} is the mass of each element, $\mathbf{I_{E_i}}$ its inertia, $h_{CM_{E_i}}$ the z coordinate of the center of mass position, $\mathbf{v_{CM_{E_i}}}$ the linear velocity of the center of mass and $\omega_{\mathbf{CM_{E_i}}}$ its angular velocity. The position of the center of mass of each element $\mathbf{CM_E}$ is shown in Fig. 14,

$$\begin{aligned}
\mathbf{CM_{E_1}} &= \mathbf{P_{Tr}} + \mathbf{l_{CM_{E_1}}} \\
\mathbf{CM_{E_2}} &= \mathbf{P_{Tr}} + \mathbf{l_3} + \mathbf{l_4} + \mathbf{d_1} - \mathbf{l_{CM_{E_2}}} \\
\mathbf{CM_{E_3}} &= \mathbf{P_{Tr}} + \mathbf{l_3} + \mathbf{l_4} + \mathbf{d_1} + \mathbf{l_{CM_{E_3}}} \\
\mathbf{CM_{E_4}} &= \mathbf{P_{Tr}} + \mathbf{l_3} + \mathbf{l_{10}} + \mathbf{l_9} + \mathbf{l_{CM_{E_4}}} \\
\mathbf{CM_{E_5}} &= \mathbf{P_{Tr}} + \mathbf{l_3} + \mathbf{l_{10}} + \mathbf{l_{CM_{E_5}}}
\end{aligned} \tag{45}$$

The linear velocity ($\mathbf{v_{CM_{E_i}}}$) is obtained by differentiating $\mathbf{CM_{E_i}}$,

$$\mathbf{v_{CM_{E_i}}} = \frac{\partial \mathbf{CM_{E_i}}}{\partial \mathbf{P_{Tr}}} \dot{\mathbf{P}}_{\mathbf{Tr}} \tag{46}$$

On the other hand, the angular velocities are calculated in terms of the passives variables,

$$\omega_{\mathbf{CM_{E_1}}} = \omega_{\mathbf{CM_{E_2}}} = \omega_{\mathbf{CM_{E_3}}} = \begin{bmatrix} -\dot{\varphi}_1 \cos(\alpha) \\ -\dot{\alpha} \\ -\dot{\varphi}_1 \sin(\alpha) \end{bmatrix} \tag{47}$$

$$\omega_{\mathbf{CM_{E_4}}} = \begin{bmatrix} -\dot{\varphi}_3 \cos(\alpha) \\ -\dot{\alpha} \\ -\dot{\varphi}_3 \sin(\alpha) \end{bmatrix} \tag{48}$$

$$\omega_{\mathbf{CM_{E_5}}} = \begin{bmatrix} -\dot{\varphi}_2 \cos(\alpha) \\ -\dot{\alpha} \\ -\dot{\varphi}_2 \sin(\alpha) \end{bmatrix} \tag{49}$$

Combining Eqs. 43-49, kinetic and potential energies are defined in terms of the transmission motion ($\mathbf{P_{Tr}}$), the dependent variables ($\mathbf{q_{na_A}}$) and their derivatives ($\dot{\mathbf{P}}_{\mathbf{Tr}}$, $\dot{\mathbf{q}}_{\mathbf{na_A}}$). So, the Lagrangian function of the Pantograph will depend on these two sets of variables ($L(\mathbf{P_{Tr}}, \dot{\mathbf{P}}_{\mathbf{Tr}}, \mathbf{q_{na_A}}, \dot{\mathbf{q}}_{\mathbf{na_A}})$).

Applying the Lagrangian formulation (Eq. 42),

$$\begin{aligned} \mathbf{D_{Tr}}\ \ddot{\mathbf{P}}_{\mathbf{Tr}} + \mathbf{C_{Tr}}\ \dot{\mathbf{P}}_{\mathbf{Tr}} + \mathbf{G_{Tr}} &= \frac{d}{dt}\left(\frac{\partial \mathbf{L}}{\partial \dot{\mathbf{P}}_{\mathbf{Tr}}}\right) - \frac{\partial \mathbf{L}}{\partial \mathbf{P_{Tr}}} \\ &= \sum \lambda_{Tr} \frac{\partial \mathbf{\Gamma_{Tr}}(\mathbf{P_{Tr}}, \mathbf{q_{na_A}})}{\partial \mathbf{P_{Tr}}} + \mathbf{F_{Tr}} \end{aligned} \tag{50}$$

$$\begin{aligned} \mathbf{D_q}\ \ddot{\mathbf{q}}_{\mathbf{na_A}} + \mathbf{C_q}\ \dot{\mathbf{q}}_{\mathbf{na_A}} + \mathbf{G_q} &= \frac{d}{dt}\left(\frac{\partial \mathbf{L}}{\partial \dot{\mathbf{q}}_{\mathbf{na_A}}}\right) - \frac{\partial \mathbf{L}}{\partial \mathbf{q_{na_A}}} \\ &= \sum \lambda_{Tr} \frac{\partial \mathbf{\Gamma_{Tr}}(\mathbf{P_{Tr}}, \mathbf{q_{na_A}})}{\partial \mathbf{q_{na_A}}} \end{aligned} \tag{51}$$

where, $\mathbf{\Gamma_{Tr}}(\mathbf{P_{Tr}}, \mathbf{q_{na_A}}) = \mathbf{0}$ is the closure equation that relates the input and output variables (Eq. 29), λ_{Tr} is the set of Lagrange multipliers, and $\mathbf{F_{Tr}}$ is the force applied in the transmission point ($\mathbf{P_{Tr}}$). On the other hand, inertia $\mathbf{D}$, Coriolis $\mathbf{C}$ and gravity $\mathbf{G}$ terms, which depends on the dependant variables ($\mathbf{D_q}$, $\mathbf{C_q}$ and $\mathbf{G_q}$) or transmission motion ($\mathbf{D_{Tr}}$, $\mathbf{C_{Tr}}$ and $\mathbf{G_{Tr}}$), can be easily defined by grouping acceleration, velocity and gravitational terms.

If the model is to be defined in terms of $\mathbf{P_{Tr}}$, and considering that $\mathbf{J_{q_{na_A}}} = \partial \mathbf{q_{na_A}} / \partial \mathbf{P_{Tr}}$ (Eq. 41),

$$\mathbf{F_{Tr}} = \mathbf{D_{Tr}} \ddot{\mathbf{P}}_{\mathbf{Tr}} + \mathbf{C_{Tr}} \dot{\mathbf{P}}_{\mathbf{Tr}} + \mathbf{G_{Tr}} + \mathbf{J_{q_{na_A}}}^T (\mathbf{D_q} \ddot{\mathbf{q}}_{\mathbf{na_A}} + \mathbf{C_q} \dot{\mathbf{q}}_{\mathbf{na_A}} + \mathbf{G_q}) - \mathbf{J_x}^T \mathbf{F_{Cn}} \tag{52}$$

which can be rewritten in compact form in terms of $\mathbf{P_{Tr}}$ and its velocity and acceleration,

$$\mathbf{F_{Tr}} = \mathbf{D}\ \ddot{\mathbf{P}}_{Tr} + \mathbf{C}\ \dot{\mathbf{P}}_{Tr} + \mathbf{G} + \mathbf{F_E} \tag{53}$$

where,

$$\begin{aligned}
\mathbf{D} &= \mathbf{D_{Tr}} + \mathbf{J_{q_{na_A}}}^T \mathbf{D_q} \mathbf{J_{q_{na_A}}} \\
\mathbf{C} &= \mathbf{C_{Tr}} + \mathbf{J_{q_{na_A}}}^T \mathbf{C_q} \mathbf{J_{q_{na_A}}} + \mathbf{J_{q_{na_A}}}^T \mathbf{D_q} \dot{\mathbf{J}}_{\mathbf{q_{na_A}}} \\
\mathbf{G} &= \mathbf{G_{Tr}} + \mathbf{J_{q_{na_A}}}^T \mathbf{G_q} \\
\mathbf{F_E} &= -\mathbf{J_x}^T \mathbf{F_{Cn}}
\end{aligned} \tag{54}$$

Thus, the relationship between the interaction force ($\mathbf{F_{Cn}}$) and dynamical behavior ($\mathbf{F_{Tr}}$ and $\mathbf{P_{Tr}}$) of the transmission point is obtained by Eq.54.

5. Experimental Validation

Several experimental tests were carried out to demonstrate the effectiveness of the identified kinematical and dynamical models of the UHP rehabilitation robot. With this objective, the defined models were implemented in Matlab, and its results were compared with data obtained from experimental tests with the UHP prototype.

For that purpose, in addition to the sensors included in the prototype, (i.e. the encoders measuring motor rotation angle ($\mathbf{q_m}$) and the linear potentiometers used to determine the lengths of upper springs (n_{S_A} and n_{S_B})), a force sensor (MINI40, ATI) and a 3 axis inclinometer (YNGS1, Sensor-Technik Wiedemann GmbH) were added to the actuated bar. The force sensor, which was located in the contact point ($\mathbf{P_{Cn}}$), was used to measure the contact force ($\mathbf{F_{Cn}}$), while the inclinometer, measuring the actuated bar inclination in x and y axes, allows to precisely estimate the contact point motion ($\mathbf{P_{Cn}}$).

The motor controllers, prototype sensors and extra sensors were connected to a centralized embedded controller based on CompactRIO platform. The data acquisition system was implemented in Labview Real-Time.

The distance parameters of the UHP were experimentally identified, while the motor-pulley parameters (Eq. 19) were identified using the Grey-box procedure [34]. And the Pantograph mass and inertia were obtained from combining real measurements and MSC ADAMS multibody simulation software. The parameters of the UHP are summarized in Table 1.

Parameter	**Value**	**Parameter**	**Value**
I_{m_1}	$0.003615 Ns^2/rad$	l_6	$0.202m$
I_{m_2}	$0.002742 Ns^2/rad$	l_7	$0.12m$
B_{m_1}	$1.02 \cdot 10^{-7} Ns/rad$	l_8	$0.268m$
B_{m_2}	$5.27 \cdot 10^{-9} Ns/rad$	l_9	$0.662m$
F_{c_1}	$0.840395 Nm$	l_{10}	$0.268m$
F_{c_2}	$0.731213 Nm$	$l_{CM_{E_1}}$	$0.17m$
β_1	$4223.98s$	$l_{CM_{E_2}}$	$0.21m$
β_2	$4318.25s$	$l_{CM_{E_3}}$	$0.101m$
r_{p_1}	$0.047m$	$l_{CM_{E_4}}$	$0.134m$
r_{p_2}	$0.0325m$	$l_{CM_{E_5}}$	$0.331m$
l_{0_A}	$0.035m$	m_{E_1}	$0.882kg$
l_{0_B}	$0.032m$	m_{E_2}	$1.25kg$
l_{0_C}	$0.038m$	m_{E_3}	$1.23kg$
l_{0_D}	$0.031m$	m_{E_4}	$1.55kg$
k_{S_i}	$4000N/m$	m_{E_5}	$1.17kg$
l_1	$0.575m$	I_{E_1}	$[13.5 \;\; 0.49 \;\; 13.4\,]\ 10^{-3} kg\ m^2$
l_2	$0.15m$	I_{E_2}	$[\,9.7 \;\; 0.59 \;\; 9.51]\ 10^{-3} kg\ m^2$
l_3	$0.18m$	I_{E_3}	$[\,4.9 \;\; 1.96 \;\; 3.61]\ 10^{-3} kg\ m^2$
l_4	$0.46m$	I_{E_4}	$[\,40 \;\; 13.5 \;\; 28\,]\ 10^{-3} kg\ m^2$
l_5	$0.64m$	I_{E_5}	$[\,31 \;\; 0.53 \;\; 31\,]\ 10^{-3} kg\ m^2$

Table 1: Parameters of the UHP prototype.

Four tests were carried out to validate the kinematical and dynamical models of UHP rehabilitation robot. In order to show that the models work correctly when the robot interacts with the user, the experimental tests were performed with healthy people. It is noted that 75 experiments were carried out, and that only the most significative results are shown to demonstrate the validity of the models.

First, the kinematical models of the drive system SEA (Section 3.1) and the Pantograph in ARM mode (Section 4.1) were validated. For this purpose, the motors executed a 5s period sinusoidal motion without external force. This means that the user did not execute any resistive force to the movement of the motors. The motor rotation angles ($\mathbf{q_m}$) and variable length of the upper springs (n_{S_A} and n_{S_B}) were used to estimate the contact motion ($\mathbf{P_{Cn}}$). In order to validate the estimation, $\mathbf{P_{Cn}}$ was also calculated from the inclinometer measurements.

In Fig. 15, the real and estimated values of x and y components (x_{Cn} and y_{Cn}) of $\mathbf{P_{Cn}}$ are depicted. As it can be seen, the mean error is smaller than $3mm$ and the maximum error is $6mm$. Note that the motion area of the UHP in ARM mode is a circumference of $150mm$ radius, hence, the motion error is less than 2% of the motion area and the obtained kinematical model can be used to estimate the contact motion ($\mathbf{P_{Cn}}$) without the need of additional sensors.

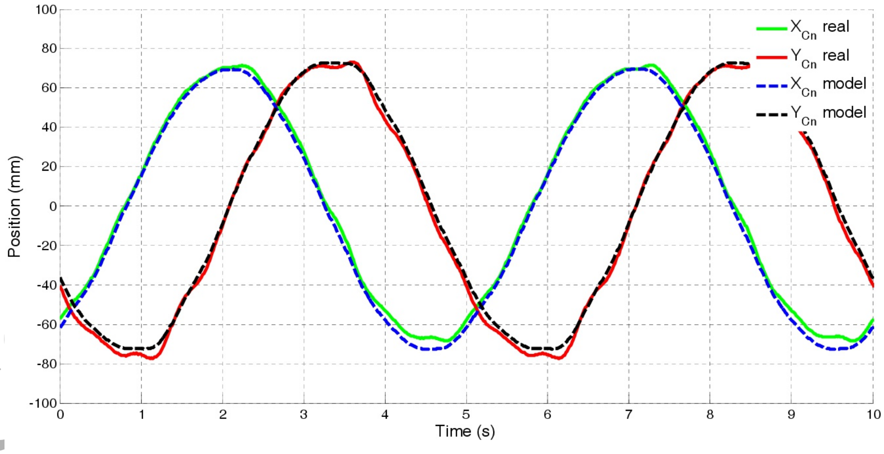

Figure 15: Kinematical model validation results.

The second test was used to validate the dynamical model of the drive system (Section 3.2). With this objective, the Pantograph was locked in the equilibrium position ($\mathbf{P_{Tr}} = [0\ 0\ 0]^T$) and the motors were induced to perform a sinusoidal motion with 5s period. The force of the sensorized upper springs (F_{S_A} and F_{S_B}) was calculated based on the motor torques ($\tau_\mathbf{m}$) and rotation angles ($\mathbf{q_m}$). These values were compared with the forces directly computed with spring constants and their length variations measured by the linear potentiometer.

Fig. 16, shows the real and estimated values of F_{S_A} and F_{S_B}. In this case, the mean error is $2N$. The springs of the UHP present a maximum variable length ($\mathbf{n_S}$) of $30mm$, hence, with its constant (k_{S_i}) $4000N/m$, the maximum force that can apply to each spring ($F_{S_i} = k_{S_i}\ n_{S_i}$) is $\pm 120N$. Therefore, the estimation error is less than 3% of the force range of the spring.

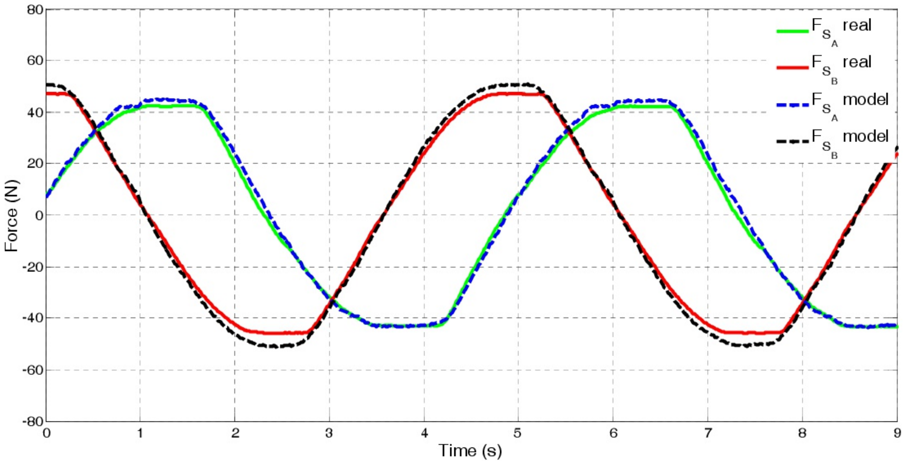

Figure 16: Dynamical model validation results: SEA based drive system.

The third experimental test was implemented to validate the transmission point ($\mathbf{P_{Tr}}$) dynamics (Section 3.3) and Pantograph dynamical model (Section 4.2). For this purpose, the motors were locked and the user moved the UHP through its motion range. The variable length of the upper springs (n_{S_A} and n_{S_B}) were used to obtain the transmission force ($\mathbf{F_{Tr}}$) based on the drive system dynamical model (Eq. 27). This estimation was compared with the measurement of the contact force ($\mathbf{F_{Cn}}$) and the use of the dynamical model of the Pantograph.

Fig. 17 shows the values of $\mathbf{F_{Tr}}$ calculated with both the dynamical models of the SEA based drive system and the Pantograph in ARM mode. As it can be observed, the mean error is smaller than $5N$. In a robust and safe robot operation, the contact point impedance of the UHP in ARM mode should be less than $400N/m$, so the contact force ($\mathbf{F_{Cn}}$) oscillates in the range $\pm 60N$. Considering the geometry of the Pantograph, the estimated transmission force ($\mathbf{F_{Tr}}$) range is 3.2 times wider than the contact force ($\mathbf{F_{Cn}}$) range so the maximum $\mathbf{F_{Tr}}$ becomes $\pm 192N$. Hence, the mean error is less than %3, while the maximum error is smaller than 10% of the maximum force range.

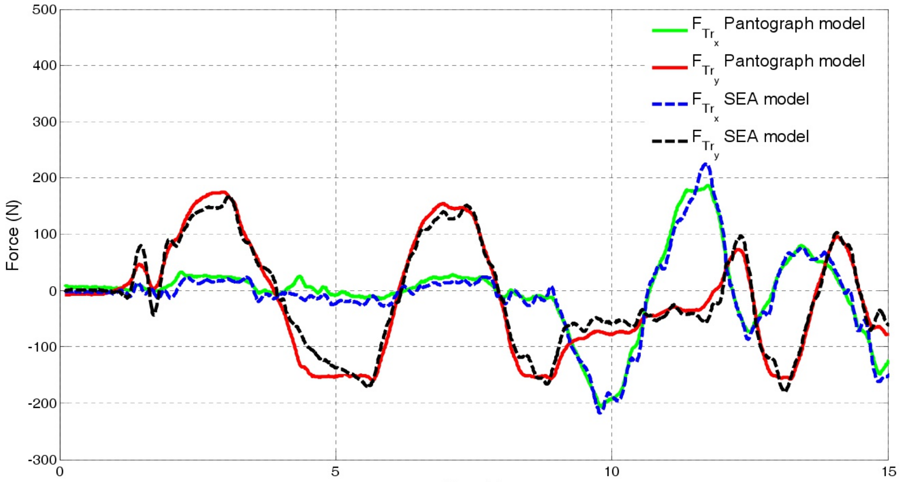

Figure 17: Dynamical model validation results: Pantograph structure.

In the previous tests, the kinematical and dynamical models of the SEA drive system and Pantograph were validated separately under specific constrained motions of the robot. In the fourth and last test, the whole system was validated. For that purpose, the drive system was induced to perform a sinusoidal motion with 5s period, while the user tried to maintain the robot as close to the origin as possible.

For that purpose, the motor rotation angles ($\mathbf{q_m}$) and the variable length of the upper springs (n_{S_A} and n_{S_B}) were used to calculate the motion of the contact point ($\mathbf{P_{Cn}}$), which was compared with the actual values reconstructed with the inclinometer signals. In addition, the transmission force $\mathbf{F_{Tr}}$ was obtained based on the drive systems model, and with the force sensors measures and the use of the dynamical model of the Pantograph.

In Fig. 18, the real and estimated values of $\mathbf{P_{Cn}}$ are observed. As it can be extracted from the experimental data, the mean error is smaller than $3mm$ and the maximum error is $10mm$. As mentioned previously, motion area of the UHP in ARM mode is a circumference of 150mm radius, hence, the motion error is less than 3.34% of the motion area.

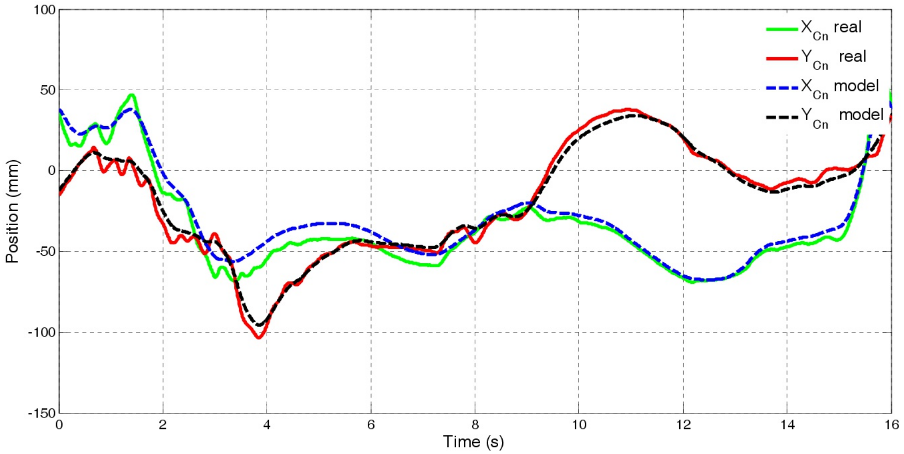

Figure 18: Kinematical validation results of UHP model.

Fig. 19 shows the values of $\mathbf{F_{Tr}}$ calculated with both the dynamical models of the SEA based drive system and the Pantograph in ARM mode. As it can be seen, the mean error is smaller than 10% of the maximum force range.

It is noted that in health and care applications such as rehabilitation, movement accuracy is not as critical as in other applications like surgery. In the literature [36], the position resolution that healthy humans can control during upper limbs movement is $5mm$ in the average, indicating that the mean error of $3mm$ is higher than the resolution of human arm movement. Moreover, in the most of actual robot mediated trainings using force, the force magnitude is

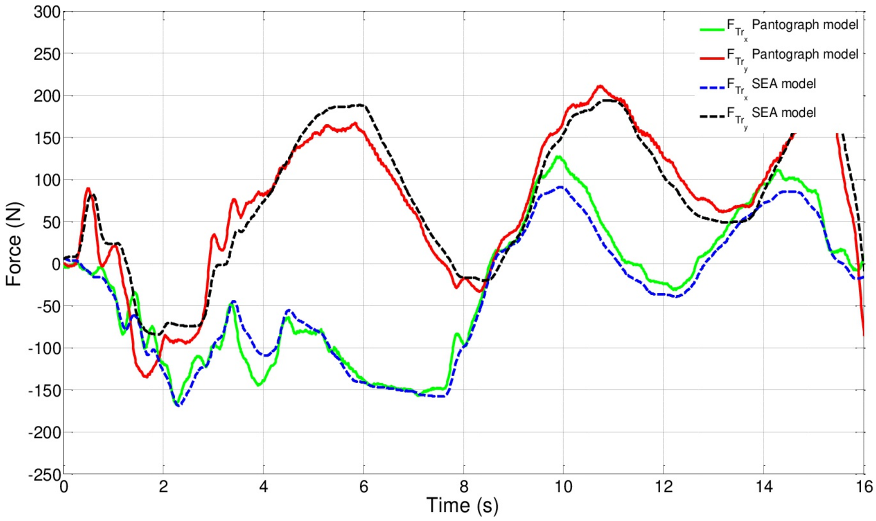

Figure 19: Dynamical validation results of UHP model.

smaller than $20N$ for the patient safety [37], which means force errors of 10% correspond to $2N$. In this sense, the position and force errors obtained in this study are likely to be acceptable in the use for rehabilitation purpose.

6. Conclusions

In this paper, kinematical and dynamical models of the multipurpose rehabilitation robot, Universal Haptic Pantograph (UHP) have been identified. This work focuses on the ARM mode which is used for impaired elbow and shoulder rehabilitation, among different rehabilitation modes offered by UHP thanks to its reconfigurable mechanical structure.

The UHP structure can be divided in two subsystems: a SEA based drive system, and a Pantograph structure with which the user interacts. These two subsystems are connected through the transmission point, allowing the control of motion and force of UHP depending on the purpose of the rehabilitation program. Based on the loop vector equations and the Lagrangian formulation, the kinematical and dynamical models of both subsystems have been derived, aiming to estimate system outputs with the minimum of required sensors as well as facilitate the design of advanced interaction controllers between user and UHP.

In order to demonstrate the validity of the model and its application as motion and force estimators, several experimental tests were carried out. For the validation, the system outputs estimated using the models were compared with those obtained by measurements. The results demonstrate that the motion mean error in the contact point ($\mathbf{P_{Cn}}$) is less than 4% of the motion area, while the transmission force ($\mathbf{F_{Tr}}$) error is smaller than the 10% of maximum force range. Moreover, these results imply that the models can be used in the estimation of the system outputs as well as in the design of the controller with acceptable accuracy and reliability for rehabilitation applications as the obtained accuracy is higher than human motion and force resolution. Therefore, it is concluded that the use of the developed model can minimize required sensor sets, resulting in the reduction of the robot cost.

In future works, the proposed kinematical and dynamical models will apply to the implementation of advanced controllers for rehabilitation purpose. And the control performance will be compared with that based on direct measurement of force and motion while interacting with the user.

Acknowledgements

This work was supported in part by the Basque Country Governments (GV/EJ) under grant PRE-2014-1-152, UPV/EHU's PPG17/56 project, Basque Country Governments IT914-16 project, Spanish Ministry of Economy and Competitiveness' MINECO & FEDER inside DPI-2012-32882 projects, Spanish Ministry of Economy and Competitiveness BES-2013-066142 grant, Euskampus, FIK and Spanish Ministry of Science and Innovation PDI-020100-2009-21 project.

References

[1] J. L. Pons, R. Raya, J. González, Emerging Therapies in Neurorehabilitation II, Vol. 10 of Biosystems & Biorobotics, Springer International Publishing, Cham, (2016) 29–64. `doi:10.1007/978-3-319-24901-8`.

[2] Z. Corbyn, Statistics: A growing global burden, Nature 510 (7506) (2014) 2–3. `doi:10.1038/510S2a`.

[3] L. Sawaki, Use-dependent plasticity of the human motor cortex in health and disease, IEEE Engineering in Medicine and Biology Magazine 24 (1) (2005) 36–39. `doi:10.1109/MEMB.2005.1384098`.

[4] N. Norouzi-Gheidari, P. S. Archambault, J. Fung, Effects of robot-assisted therapy on stroke rehabilitation in upper limbs: Systematic review and meta-analysis of the literature, Journal of Rehabilitation Research and Development 49 (4) (2012) 479–495. `doi:10.1682/JRRD.2010.10.0210`.

[5] P. Maciejasz, J. Eschweiler, K. Gerlach-Hahn, A. Jansen-Troy, S. Leonhardt, A survey on robotic devices for upper limb rehabilitation, Journal of neuroengineering and rehabilitation 11:3 (1) (2014) 1–29. `doi:10.1186/1743-0003-11-3`.

[6] R. A. R. C. Gopura, D. S. V. Bandara, K. Kiguchi, G. K. I. Mann, Developments in hardware systems of active upper-limb exoskeleton robots: A review, Robotics and Autonomous Systems 75 (2016) 203–220. `doi:10.1016/j.robot.2015.10.001`.

[7] S.-H. Zhou, J. Fong, V. Crocher, Y. Tan, D. Oetomo, I. Mareels, Learning control in robot-assisted rehabilitation of motor skills a review, Journal of Control and Decision 7706 (March) (2016) 1–25. `doi:10.1080/23307706.2015.1129295`.

[8] N. Hogan, H. Krebs, J. Charnnarong, P. Srikrishna, A. Sharon, MIT-MANUS: a workstation for manual therapy and training. I, IEEE Inter-

national Workshop on Robot and Human Communication (1992) 161–165doi:10.1109/ROMAN.1992.253895.

[9] P. S. Lum, C. G. Burgar, P. C. Shor, Evidence for improved muscle activation patterns after retraining of reaching movements with the MIME robotic system in subjects with post-stroke hemiparesis, IEEE Transactions on Neural Systems and Rehabilitation Engineering 12 (2) (2004) 186–194. doi:10.1109/TNSRE.2004.827225.

[10] F. Amirabdollahian, R. Loureiro, E. Gradwell, C. Collin, W. Harwin, G. Johnson, Multivariate analysis of the Fugl-Meyer outcome measures assessing the effectiveness of GENTLE/S robot-mediated stroke therapy., Journal of neuroengineering and rehabilitation 4:4 (2007) 1–16. doi:10.1186/1743-0003-4-4.

[11] G. Fazekas, M. Horvath, T. Troznai, A. Toth, Robot-mediated upper limb physiotherapy for patients with spastic hemiparesis: A preliminary study, Journal of Rehabilitation Medicine 39 (7) (2007) 580–582. doi:10.2340/16501977-0087.

[12] M. Mihelj, T. Nef, R. Riener, ARMin - Toward a six DoF upper limb rehabilitation robot, IEEE/RAS-EMBS International Conference on Biomedical Robotics and Biomechatronics (2006) 1154–1159doi:10.1109/BIOROB.2006.1639248.

[13] A. Frisoli, F. Salsedo, M. Bergamasco, B. Rossi, M. C. Carboncini, A force-feedback exoskeleton for upper-limb rehabilitation in virtual reality, Applied Bionics and Biomechanics 6 (2) (2009) 115–126. doi:10.1080/11762320902959250.

[14] T. G. Sugar, J. He, E. J. Koeneman, J. B. Koeneman, R. Herman, H. Huang, R. S. Schultz, D. E. Herring, J. Wanberg, S. Balasubramanian, P. Swenson, J. A. Ward, Design and control of RUPERT: A device for robotic upper extremity repetitive therapy, IEEE Transactions

on Neural Systems and Rehabilitation Engineering 15 (1) (2007) 336–346. doi:10.1109/TNSRE.2007.903903.

[15] A. Otten, C. Voort, A. Stienen, R. Aarts, E. van Asseldonk, H. van der Kooij, LIMPACT:A Hydraulically Powered Self-Aligning Upper Limb Exoskeleton, Mechatronics PP (99) (2015) 1–14. doi:10.1109/TMECH.2014.2375272.

[16] N. Jarrassé, T. Proietti, V. Crocher, J. Robertson, A. Sahbani, G. Morel, A. Roby-Brami, Robotic Exoskeletons: A Perspective for the Rehabilitation of Arm Coordination in Stroke Patients, Frontiers in Human Neuroscience 8 (947) (2014) 1–13. doi:10.3389/fnhum.2014.00947.

[17] R. Vertechy, A. Frisoli, A. Dettori, M. Solazzi, M. Bergamasco, Development of a new exoskeleton for upper limb rehabilitation, IEEE International Conference on Rehabilitation Robotics (2009) 188–193doi:10.1109/ICORR.2009.5209502.

[18] M. H. Rahman, M. J. Rahman, O. L. Cristobal, M. Saad, J. P. Kenné, P. S. Archambault, Development of a whole arm wearable robotic exoskeleton for rehabilitation and to assist upper limb movements, Robotica (2014) 19–39doi:10.1017/S0263574714000034.

[19] Z. Song, S. Zhang, B. Gao, Implementation of Resistance Training Using an Upper-Limb Exoskeleton Rehabilitation Device for Elbow Joint, Journal of Medical and Biological Engineering 34 (2) (2013) 188–196. doi:10.5405/jmbe.1337.

[20] K. Kiguchi, Y. Hayashi, An EMG-based control for an upper-limb power-assist exoskeleton robot, IEEE Transactions on Systems, Man, and Cybernetics 42 (4) (2012) 1064–1071. doi:10.1109/TSMCB.2012.2185843.

[21] N. Hogan, Impedance Control: An Approach to Manipulation: Part I Theory, Journal of Dynamic Systems, Measurement, and Control 107 (1985) 1–27. doi:10.1115/1.3140702.

[22] M. Babaiasl, S. H. Mahdioun, P. Jaryani, M. Yazdani, A review of technological and clinical aspects of robot-aided rehabilitation of upper-extremity after stroke, Disability and Rehabilitation: Assistive Technology (2015) 1–18`doi:10.3109/17483107.2014.1002539`.

[23] N. Nordin, S. Q. Xie, B. Wünsche, Assessment of movement quality in robot- assisted upper limb rehabilitation after stroke: a review, Journal of NeuroEngineering and Rehabilitation 11:137 (1) (2014) 1–23. `doi:10.1186/1743-0003-11-137`.

[24] A. J. Westerveld, B. J. Aalderink, W. Hagedoorn, M. Buijze, A. C. Schouten, H. van der Kooij, A Damper Driven Robotic End-Point Manipulator for Functional Rehabilitation Exercises After Stroke, IEEE Transactions on Biomedical Engineering 61 (10) (2014) 2646–2654. `doi:10.1109/TBME.2014.2325532`.

[25] A. Song, L. Pan, G. Xu, H. Li, Adaptive motion control of arm rehabilitation robot based on impedance identification, Robotica (2014) 1–18`doi:10.1017/S026357471400099X`.

[26] S. Etedali, H. A. Talebi, A. D. Mohammadi, A robust force observer for robot manipulators subjected to external disturbance, International Conference on Robotics and Mechatronics (ICROM) (2015) 539–544`doi:10.1109/ICRoM.2015.7367841`.

[27] H. Amini, V. Dabbagh, S. M. Rezaei, M. Zareinejad, N. A. Mardi, A. A. D. Sarhan, Robust control-based linear bilateral teleoperation system without force sensor, Journal of the Brazilian Society of Mechanical Sciences and Engineering 37 (2) (2015) 579–587. `doi:10.1007/s40430-014-0207-2`.

[28] M. Linderoth, A. Stolt, A. Robertsson, R. Johansson, Robotic force estimation using motor torques and modeling of low velocity friction disturbances, IEEE/RSJ International Conference on Intelligent Robots and Systems (2013) 3550–3556`doi:10.1109/IROS.2013.6696862`.

[29] J. Oblak, Z. Matjačić, Design of a series visco-elastic actuator for multi-purpose rehabilitation haptic device, Journal of neuroengineering and rehabilitation 8 (3) (2011) 1–13. `doi:10.1186/1743-0003-8-3`.

[30] J. C. Perry, J. Oblak, J. H. Jung, I. Cikajlo, J. F. Veneman, N. Goljar, N. Bizoviar, Z. Matjačić, T. Keller, Variable structure pantograph mechanism with spring suspension system for comprehensive upper-limb haptic movement training, The Journal of Rehabilitation Research and Development 48 (4) (2011) 317. `doi:10.1682/JRRD.2010.03.0043`.

[31] J. Oblak, I. Cikajlo, Z. Matjacic, Universal Haptic Drive: A Robot for Arm and Wrist Rehabilitation, IEEE Transactions on Neural Systems and Rehabilitation Engineering 18 (3) (2010) 293–302. `doi:10.1109/TNSRE.2009.2034162`.

[32] G. Pratt, M. Williamson, Series elastic actuators, IEEE/RSJ International Conference on Intelligent Robots and Systems. Human Robot Interaction and Cooperative Robots (1995) 399–406`doi:10.1109/IROS.1995.525827`.

[33] K. Kong, J. Bae, M. Tomizuka, Control of rotary series elastic actuator for ideal force-mode actuation in human-robot interaction applications, IEEE/ASME Transactions on Mechatronics 14 (1) (2009) 105–118. `doi:10.1109/TMECH.2008.2004561`.

[34] E. Wernholt, S. Gunnarsson, Nonlinear Identification of a Physically Parameterized Robot Model, IFAC Proceedings Volumes 39 (1) (2006) 143–148. `doi:10.3182/20060329-3-AU-2901.00016`.

[35] H. Chen, Y. Liu, Robotic assembly automation using robust compliant control, Robotics and Computer-Integrated Manufacturing 29 (2) (2013) 293–300. `doi:10.1016/j.rcim.2012.09.001`.

[36] M. Germanotta, G. Vasco, M. Petrarca, S. Rossi, S. Carniel, E. Bertini, P. Cappa, E. Castelli, Robotic and clinical evaluation of upper limb motor performance in patients with Friedreich Ataxia: an observational study,

Journal of NeuroEngineering and Rehabilitation 12 (41) (2015) 1–13. `doi:10.1186/s12984-015-0032-6`.

[37] C. Ochoa Luna, M. H. Rahman, M. Saad, P. Archambault, W.-H. Zhu, Virtual decomposition control of an exoskeleton robot arm, Robotica 34 (07) (2016) 1587–1609. `doi:10.1017/S026357471400246X`.